

Neural Point Estimation for Fast Optimal Likelihood-Free Inference

Matthew Sainsbury-Dale¹, Andrew Zammit-Mangion¹, and Raphaël Huser²

¹School of Mathematics and Applied Statistics, University of Wollongong, Australia

²Statistics Program, Computer, Electrical and Mathematical Sciences and Engineering Division, King Abdullah University of Science and Technology (KAUST), Saudi Arabia

Abstract

Neural point estimators are neural networks that map data to parameter point estimates. They are fast, likelihood free and, due to their amortised nature, amenable to fast bootstrap-based uncertainty quantification. In this paper, we aim to increase the awareness of statisticians to this relatively new inferential tool, and to facilitate its adoption by providing user-friendly open-source software. We also give attention to the ubiquitous problem of making inference from replicated data, which we address in the neural setting using permutation-invariant neural networks. Through extensive simulation studies we show that these neural point estimators can quickly and optimally (in a Bayes sense) estimate parameters in weakly-identified and highly-parameterised models with relative ease. We demonstrate their applicability through an analysis of extreme sea-surface temperature in the Red Sea where, after training, we obtain parameter estimates and bootstrap-based confidence intervals from hundreds of spatial fields in a fraction of a second.

Keywords: amortised inference, Bayes estimator, deep learning, exchangeable data, extreme-value model, permutation invariant, spatial statistics

1 Introduction

The most popular methods for making inference with parametric statistical models are those based on the likelihood function, but a number of challenges can preclude their use. First, the likelihood function may be unavailable. For example, it is typically not possible to formulate the likelihood function for implicit generative (simulator) models (Diggle and Gratton, 1984, Lintusaari et al., 2017). Second, even if the likelihood function is available, it may be computationally intractable. For example, popular models for spatial extremes are max-stable processes, for which the number of terms involved in the likelihood function grows more

than exponentially fast with the number of observation locations (e.g., Padoan et al., 2010, Huser et al., 2019). One proposed solution is to replace the full likelihood with a composite likelihood (e.g., Cox and Reid, 2004, Varin and Vidoni, 2005, Varin et al., 2011), but this usually results in a loss of statistical efficiency (Huser and Davison, 2013, Castruccio et al., 2016), and it is not always clear how to optimally select composite likelihood components. The related Vecchia approximation (Vecchia, 1988) has been applied successfully both in the Gaussian (e.g., Stein et al., 2004) and max-stable (Huser et al., 2022) settings, but this approach is still an approximation that faces a trade-off between computational and statistical efficiency. Several fast approximate methods have been developed to fit latent Gaussian process models, such as the integrated-nested Laplace approximation (INLA; Rue et al., 2009) or Max-and-Smooth (Hrafnkelsson et al., 2021), but these methods only apply to this specific model class.

Several likelihood-free methods have been developed to bypass these challenges, the most popular of which is approximate Bayesian computation (ABC; Beaumont et al., 2002, Sisson et al., 2018). In its simplest form, ABC involves sampling parameters from the prior, simulating from the model, and retaining parameters as an approximate sample from the posterior if the simulated data are “similar” to the observed data, with similarity typically assessed by comparing low-dimensional summary statistics. ABC is sensitive to the choice of summary statistics, which traditionally require expert knowledge to construct. Although deep learning methods can alleviate this specific dependence on expert knowledge by automatically learning relevant summary statistics (e.g., Jiang et al., 2017, Raynal et al., 2018, Wqvist et al., 2019, Chen et al., 2021), ABC methods remain difficult to calibrate, as the number of summary statistics, the tolerance used when comparing statistics, and the strength of prior information, each represent a trade-off between computational and statistical efficiency. Sequential Monte Carlo (Sisson et al., 2007) and Markov-chain Monte Carlo (Sisson and Fan, 2011) variants aim to alleviate these trade-offs by optimising sampling from the proposal distribution, but calibration often remains difficult. Finally, ABC (and likelihood-based) methods are case-specific, in the sense that they generally involve substantial computation each time they are employed, and their run-time can vary greatly with the observed data.

Recently, neural networks have been used to directly approximate posterior distributions over parameters. Some of these *neural posterior approximators* are amortised, in the sense that a moderate upfront cost is paid to train these networks but, once trained, inference with observed data is extremely fast and with a fixed run-time. Chan et al. (2018), for example, use a neural network to estimate the parameters of a tractable variational approximation of the posterior. Normalising flows, on the other hand, model complex distributions by an invertible transformation of a simple one (Papamakarios et al., 2021), and they allow both sampling and explicit density evaluation of the approximate posterior (Radev et al., 2022). Generative adversarial networks drop invertibility in favour of increased flexibility (Ramesh et al., 2022, Pacchiardi and Dutta, 2022), but they are notoriously difficult to train.

In this work, we focus on neural networks that map data to parameter point estimates; we refer to such neural networks as *neural point estimators*. Neural point estimators date back to at least Chon and Cohen (1997), but they have only been adopted widely in recent years, for example in applications involving models for population-genetics (Flagel et al., 2018); time series (Rudi et al., 2021); spatial fields (Gerber and Nychka, 2021, Lenzi et al., 2021); spatio-temporal fields (Zammit-Mangion and Wikle, 2020); and agent-based models

(Gaskin et al., 2023). Our reasons for considering point estimators (as opposed to posterior approximators) are threefold. First, learning a point summary of the posterior distribution is an easier task than learning an entire posterior distribution and, therefore, neural point estimators are far simpler to construct and train than neural posterior approximators, and hence more likely to be used by practitioners. Second, point estimation is extensively used in statistical applications. For example, in empirical hierarchical models (e.g., Cressie and Wikle, 2011, Sec. 2.1.2) some parameters in a hierarchy are estimated and subsequently treated as known when computing posterior predictive distributions over other unknown quantities. Third, neural point estimators are (in our experience) relatively insensitive to the specific network architecture employed, which makes them ideally placed for use in general-purpose software packages. As is typically done with point estimators, uncertainty quantification of the parameters proceeds naturally through the bootstrap distribution, which is essentially available “for free” with neural point estimators. As we shall show, when properly constructed, neural point estimators approximate Bayes estimators and, in this case, we refer to them as *neural Bayes estimators*.

Inference from replicated data is commonly required in statistical applications, and we therefore give this topic particular attention. Neural point estimation with replicated data is not straightforward; for example, Gerber and Nychka (2021) considered two approaches to handling replicated data, both with drawbacks. In their first approach, they trained a neural point estimator for a single spatial field, applied it to each field independently, and averaged the resulting estimates. This approach does not reduce the bias commonly seen in optimal small-sample estimators as the sample size increases, and it is futile when the parameters are unidentifiable from a single replicate. In their second approach, they adapted the size of the neural estimator’s input layer to match the number of independent replicates. The resulting estimator is not invariant to the ordering of the replicates, it results in an explosion of neural-network parameters with increasing number of replicates, and it requires a different architecture for every possible sample size, which reduces its applicability.

In this paper, we first clarify the connection between neural point estimators and classical Bayes estimators, which is sometimes misconstrued or ignored in the literature. Second, we propose a way to do neural Bayes estimation from independent replicates by leveraging permutation-invariant neural networks, constructed using the DeepSets framework (Zaheer et al., 2017). DeepSets has been used for neural posterior approximation (e.g., Chan et al., 2018, Radev et al., 2022) but, to the best of our knowledge, this paper is the first to explore its use and the related practical considerations in a point estimation context. We show that these architectures lead to a substantial improvement in estimation accuracy when compared to those that do not account for replication appropriately. Third, we discuss important practicalities for designing and training neural Bayes estimators and, in particular, we describe a way to construct an estimator that performs optimally in the presence of variable sample sizes. For illustration, we estimate parameters in Gaussian and max-stable processes, as well as the highly-parameterised spatial conditional extremes model (Wadsworth and Tawn, 2022). We use the latter model in the analysis of sea-surface temperature extremes in the Red Sea where, using a neural Bayes estimator, we obtain estimates and bootstrap confidence intervals from hundreds of spatial fields in a fraction of a second. A primary motivation of this work is to facilitate the adoption of neural point estimation by statisticians and, to this end, we accompany the paper with user-friendly open-source software in the Julia

(Bezanson et al., 2017) and R (R Core Team, 2023) programming languages (available at [<LinksToBeInsertedHere>](#)) that can be used in a wide range of applied settings.*

The remainder of this paper is organised as follows. In Section 2, we outline the theory underlying neural Bayes estimation. In Section 3, we discuss key practical considerations when constructing neural Bayes estimators. In Section 4, we conduct extensive simulation studies that clearly illustrate the utility of neural Bayes estimators for parameter estimation. In Section 5, we use the spatial conditional extremes model to analyse sea-surface temperature in the Red Sea. In Section 6, we conclude and outline avenues for future research. A supplement is also available that contains more details and figures.

2 Methodology

In Section 2.1, we review Bayes estimators. In Section 2.2, we outline neural point estimators and discuss their connection to Bayes estimators. In Section 2.3, we discuss the use of permutation-invariant neural networks for neural Bayes estimation from replicated data.

2.1 Bayes Estimators

A statistical model is a set of probability distributions \mathcal{P} on a sample space \mathcal{S} . A parametric statistical model is one where the probability distributions in \mathcal{P} are parameterised via some p -dimensional parameter vector $\boldsymbol{\theta}$, so that $\mathcal{P} \equiv \{P_{\boldsymbol{\theta}} : \boldsymbol{\theta} \in \Theta\}$, with Θ the parameter space (McCullagh, 2002). Suppose that we have m mutually independent realisations from $P_{\boldsymbol{\theta}} \in \mathcal{P}$, which we collect in $\mathbf{Z} \equiv (\mathbf{Z}'_1, \dots, \mathbf{Z}'_m)'$. Then, the goal of parameter point estimation is to infer the unknown $\boldsymbol{\theta}$ from \mathbf{Z} using an estimator,

$$\hat{\boldsymbol{\theta}} : \mathcal{S}^m \rightarrow \Theta,$$

a mapping from m independent realisations from $\mathcal{P}_{\boldsymbol{\theta}}$ to the parameter space. Throughout, we notate estimators with parentheses to stress that they are functions of the data and, as we will see in Section 2.2, possibly also of neural-network parameters.

Estimators can be constructed intuitively within a decision-theoretic framework. Consider a non-negative loss function, $L(\boldsymbol{\theta}, \hat{\boldsymbol{\theta}}(\mathbf{Z}))$, which assesses an estimator $\hat{\boldsymbol{\theta}}(\cdot)$ for a given $\boldsymbol{\theta}$ and data set \mathbf{Z} . The estimator's risk function is the loss averaged over all possible data realisations. Assume, without loss of generality, that the sample space is $\mathcal{S} = \mathbb{R}^n$. Then, the risk function is

$$R(\boldsymbol{\theta}, \hat{\boldsymbol{\theta}}(\cdot)) \equiv \int_{\mathcal{S}^m} L(\boldsymbol{\theta}, \hat{\boldsymbol{\theta}}(\mathbf{Z})) p(\mathbf{Z} | \boldsymbol{\theta}) d\mathbf{Z}, \quad (1)$$

where $p(\mathbf{Z} | \boldsymbol{\theta}) = \prod_{i=1}^m p(\mathbf{Z}_i | \boldsymbol{\theta})$ is the likelihood function. A ubiquitous approach in estimator design is to minimise a weighted summary of (1) known as the Bayes risk,

$$r_{\Omega}(\hat{\boldsymbol{\theta}}(\cdot)) \equiv \int_{\Theta} R(\boldsymbol{\theta}, \hat{\boldsymbol{\theta}}(\cdot)) d\Omega(\boldsymbol{\theta}), \quad (2)$$

*Packages will be available on [GitHub](#) after preliminary or conditional acceptance with a journal. An anonymous version of the online documentation with example usage is provided as supplementary material (please open `index.html` in any web browser).

where $\Omega(\cdot)$ is a prior measure which, for ease of exposition, we will assume admits a density $p(\cdot)$ with respect to Lebesgue measure. A minimiser of (2) is said to be a *Bayes estimator* with respect to $L(\cdot, \cdot)$ and $\Omega(\cdot)$.

Bayes estimators are theoretically attractive. For example, unique Bayes estimator are admissible and, under suitable regularity conditions and the squared-error loss, the Bayes estimator is also consistent, asymptotically normal, and asymptotically efficient (Lehmann and Casella, 1998, Ch. 5, Thm. 2.4; Ch. 6, Thm. 8.3). Further, for a large class of prior distributions, every possible set of conditions that imply consistency of the maximum likelihood (ML) estimator also imply consistency of Bayes estimators (Strasser, 1981). Unfortunately, however, Bayes estimators are often unavailable in closed form for the complex models that are typically encountered in practice, and for models that have unavailable or intractable likelihood functions.

2.2 Neural Bayes estimators

Neural networks are ideally placed to be used for point estimation since they are universal function approximators and therefore very flexible (e.g., Hornik et al., 1989, Zhou, 2018), and because they are fast, since they usually only involve simple matrix-vector operations. Importantly, it is also straightforward to train them to approximate Bayes estimators. Denote a neural point estimator by $\hat{\boldsymbol{\theta}}(\cdot; \boldsymbol{\gamma})$, where $\boldsymbol{\gamma}$ are the neural-network parameters. Then, Bayes estimators may be approximated by $\hat{\boldsymbol{\theta}}(\cdot; \boldsymbol{\gamma}^*)$, obtained by solving the optimisation problem,

$$\boldsymbol{\gamma}^* \equiv \arg \min_{\boldsymbol{\gamma}} r_{\Omega}(\hat{\boldsymbol{\theta}}(\cdot; \boldsymbol{\gamma})). \quad (3)$$

Typically, $r_{\Omega}(\cdot)$ defined in (2) cannot be directly evaluated, but it can be approximated using Monte Carlo methods. Specifically, given a set of K parameter vectors sampled from the prior $\Omega(\cdot)$ denoted by $\boldsymbol{\vartheta}$ and, for each $\boldsymbol{\theta} \in \boldsymbol{\vartheta}$, J sets of m mutually independent realisations from $P_{\boldsymbol{\theta}}$ collected in $\mathcal{Z}_{\boldsymbol{\theta}}$,

$$r_{\Omega}(\hat{\boldsymbol{\theta}}(\cdot; \boldsymbol{\gamma})) \approx \frac{1}{K} \sum_{\boldsymbol{\theta} \in \boldsymbol{\vartheta}} \frac{1}{J} \sum_{\mathbf{Z} \in \mathcal{Z}_{\boldsymbol{\theta}}} L(\boldsymbol{\theta}, \hat{\boldsymbol{\theta}}(\mathbf{Z}; \boldsymbol{\gamma})). \quad (4)$$

Therefore, the optimisation problem (3), which is typically performed using stochastic gradient descent, can be approximated using simulation from the model, but does not require evaluation or knowledge of the likelihood function. For sufficiently flexible architectures, the point estimator targets a Bayes estimator with respect to $L(\cdot, \cdot)$ and $\Omega(\cdot)$, and will therefore inherit the associated optimality properties. We therefore call the fitted neural point estimator a *neural Bayes estimator*.

Explicitly connecting neural point estimators to Bayes estimators facilitates their interpretation, and allows one to choose the loss function $L(\cdot, \cdot)$ that targets a certain point summary of the posterior distribution. For instance, the 0–1, absolute-error, and squared-error loss functions lead to the posterior mode, median, and mean, respectively. This appealing and important property of neural Bayes estimators is often overlooked when, for example, comparing their empirical performance to that of other estimators (e.g., Lenzi et al., 2021).

2.3 Neural Bayes estimators for replicated data

As discussed in Section 1, naïve approaches to constructing neural Bayes estimators for replicated data can lead to bias, an explosion in the number of neural-network parameters, and an inability to generalise to different sample sizes. We tackle these challenges by leveraging an important property of Bayes estimators for replicated data, namely that they are invariant to permutations of the replicates. We give a proof of this intuitive property in Appendix A.

The permutation-invariance property of Bayes estimators for replicated data has largely been ignored to date in the context of neural point estimation. We propose enforcing neural point estimators to be permutation invariant by couching them in the DeepSets framework (Zaheer et al., 2017), a computationally convenient special case of Janossy pooling (Murphy et al., 2019) that represents permutation-invariant functions as

$$\begin{aligned}\hat{\theta}(\mathbf{Z}) &= \phi(\mathbf{T}(\mathbf{Z})), \\ \mathbf{T}(\mathbf{Z}) &= \mathbf{a}(\{\psi(\mathbf{Z}_i) : i = 1, \dots, m\}),\end{aligned}\tag{5}$$

where $\phi : \mathbb{R}^q \rightarrow \mathbb{R}^p$ and $\psi : \mathbb{R}^n \rightarrow \mathbb{R}^q$, and $\mathbf{a} : (\mathbb{R}^q)^m \rightarrow \mathbb{R}^q$ is a permutation-invariant set function. Each $a_j(\cdot)$, $j = 1, \dots, q$, is usually chosen to be a simple aggregation function, such as elementwise addition, average, or maximum, but may also be parameterised (Soelch et al., 2019). Beyond its attractive parsimonious form, (5) has appealing theoretical properties. For example, Han et al. (2022) show that (5) can approximate any continuously differentiable permutation-invariant real-valued function for sufficiently large q ; see also Wagstaff et al. (2019, 2022) for relevant discussion.

We use the elementwise average for each $a_j(\cdot)$, $j = 1, \dots, q$, and we therefore rely on $\phi(\cdot)$ and $\psi(\cdot)$ to provide flexibility in function approximation. We model these functions using neural networks. Collect in γ the parameters of the neural networks used to model $\psi(\cdot)$ and $\phi(\cdot)$, so that $\psi(\cdot) \equiv \psi(\cdot; \gamma)$ and $\phi(\cdot) \equiv \phi(\cdot; \gamma)$ (each function depends on only a subset of γ). The corresponding estimator of the form (5) is then given by

$$\begin{aligned}\hat{\theta}(\mathbf{Z}; \gamma) &= \phi(\mathbf{T}(\mathbf{Z}; \gamma); \gamma), \\ \mathbf{T}(\mathbf{Z}; \gamma) &= \mathbf{a}(\{\psi(\mathbf{Z}_i; \gamma) : i = 1, \dots, m\}).\end{aligned}\tag{6}$$

For illustration, consider the problem of constructing a Bayes estimator for θ from data Z_1, \dots, Z_m that are independent and identically distributed (i.i.d.) according to a uniform distribution on $[0, \theta]$, where the prior $\Omega(\cdot)$ is a conjugate Pareto distribution, and where $L(\cdot, \cdot)$ is the absolute-error loss. In this case, the unique Bayes estimator is the posterior median which, for this model, is available in closed form: for a prior $\text{Pareto}(a, b)$ distribution with shape a and scale b , the posterior median is $\tilde{b}2^{1/\tilde{a}}$, where $\tilde{a} = a + m$ and $\tilde{b} = \max(Z_1, \dots, Z_m, b)$. The Bayes estimator is thus clearly invariant to permutations of the observed samples. We let $a = 4, b = 1, m = 10$, and we construct our neural Bayes estimator to have the form (6). We use three-layer neural networks to model $\phi(\cdot; \gamma)$ and $\psi(\cdot; \gamma)$, we let $J = 1$ and $K = 10^6$ in (4), and we solve (3) using stochastic gradient descent.

Figure 1 shows the kernel-smoothed distribution of the estimators (approximated using 30,000 simulations) with θ equal to the prior mean and with the sample size $m = 10$. The first mode in the distribution of the (neural) Bayes estimator is due to the point mass in

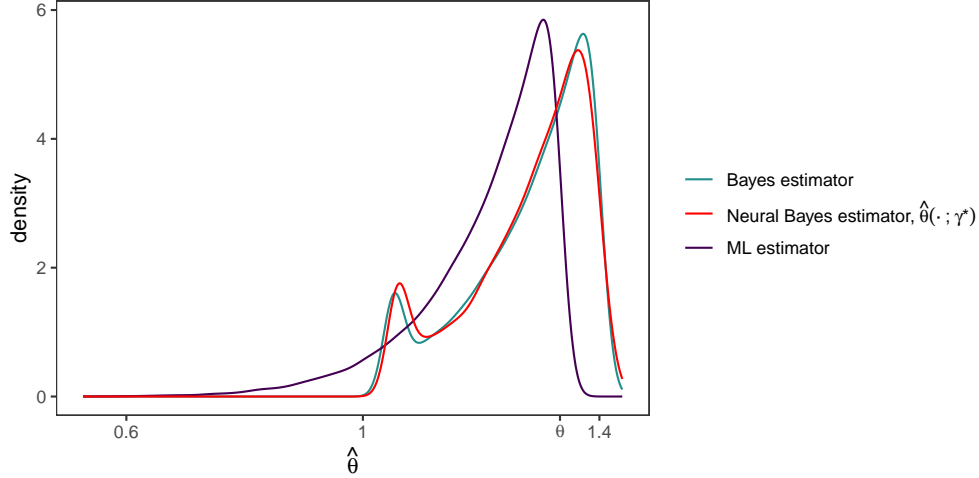


Figure 1: Kernel density approximations to the distribution of the theoretical Bayes estimator (green solid line) under the absolute-error loss, our neural Bayes estimator $\hat{\theta}(\cdot; \gamma^*)$ (red solid line) under the absolute-error loss, and the ML estimator (purple solid line) for θ from $\text{Unif}(0, \theta)$ data, where $\theta = 4/3$ is equal to the mean of the prior (Pareto) distribution, and where the sample size $m = 10$. The approximations are based on 30,000 estimates obtained through simulation.

the distribution of the posterior median resulting from the prior. We also show the kernel-smoothed distribution of the ML estimator (i.e., the sample maximum), which does not consider prior information. The distribution of our neural Bayes estimator is clearly very similar to that of the true Bayes estimator.

Finally, we note that (5) can be viewed as a nonlinear mapping of summary statistics, which is often seen in classical estimation. Indeed, best unbiased estimators for exponential family models are of the form (5) where $\mathbf{T}(\cdot)$ is sufficient for $\boldsymbol{\theta}$ (Casella and Berger, 2001, Ch. 7). This strong link to classical estimators is important, as some sufficient statistics are simple to compute, but can be difficult to model with generic neural networks. In this framework, one may therefore choose to also incorporate “expert” summary statistics, so that (6) becomes

$$\begin{aligned}\hat{\boldsymbol{\theta}}(\mathbf{Z}; \boldsymbol{\gamma}) &= \boldsymbol{\phi}(\mathbf{U}(\mathbf{Z}; \boldsymbol{\gamma}); \boldsymbol{\gamma}), \\ \mathbf{U}(\mathbf{Z}; \boldsymbol{\gamma}) &= (\mathbf{T}(\mathbf{Z}; \boldsymbol{\gamma})', \mathbf{S}(\mathbf{Z})')',\end{aligned}\tag{7}$$

where $\mathbf{S}(\cdot)$ is a q_s -vector of expert summary statistics and, in a slight abuse of notation, the domain of $\boldsymbol{\phi}(\cdot; \boldsymbol{\gamma})$ is now $(q + q_s)$ -dimensional. Equation (7) remains permutation-invariant provided that $\mathbf{S}(\cdot)$ is permutation-invariant. Since $\mathbf{T}(\cdot; \boldsymbol{\gamma})$ can theoretically approximate well any summary statistic as a smooth function of the data, the choice to include expert summary statistics in (7) is mainly a practical one that could be useful in certain applications.

3 Practical considerations

Neural Bayes estimators are conceptually simple and can be used in a wide range of problems where other approaches are computationally infeasible. They also have marked practical appeal, as the general workflow for their construction is only loosely connected to the model

being considered. The workflow for constructing a neural Bayes estimator is as follows:

- (a) Define $\Omega(\cdot)$, the prior distribution for $\boldsymbol{\theta}$.
- (b) Sample parameters from $\Omega(\cdot)$ to form sets of parameters ϑ_{train} , ϑ_{val} , and ϑ_{test} , used in (4) during the training, validation, and testing stages of the neural network, respectively.
- (c) Using the above sets of parameters, simulate data from the model, yielding the data sets $\mathcal{Z}_{\text{train}}$, \mathcal{Z}_{val} , and $\mathcal{Z}_{\text{test}}$, respectively.
- (d) Choose a loss function $L(\cdot, \cdot)$.
- (e) Design the neural network architecture for $\hat{\boldsymbol{\theta}}(\cdot; \boldsymbol{\gamma})$. If performing inference from replicated data, this involves designing architectures for $\boldsymbol{\phi}(\cdot; \boldsymbol{\gamma})$ and $\boldsymbol{\psi}(\cdot; \boldsymbol{\gamma})$ in (6).
- (f) Using $\mathcal{Z}_{\text{train}}$ and ϑ_{train} , perform the optimisation task (3) to obtain the neural Bayes estimator, $\hat{\boldsymbol{\theta}}(\cdot; \boldsymbol{\gamma}^*)$. During training, monitor progress based on \mathcal{Z}_{val} and ϑ_{val} .
- (g) Assess $\hat{\boldsymbol{\theta}}(\cdot; \boldsymbol{\gamma}^*)$ using $\mathcal{Z}_{\text{test}}$ and ϑ_{test} .

The resulting estimator then approximates a Bayes estimator with respect to $L(\cdot, \cdot)$ and $\Omega(\cdot)$. We now discuss some practical aspects of this workflow.

Defining $\Omega(\cdot)$. In addition to the usual considerations for choosing a prior measure, $\Omega(\cdot)$ here is ideally chosen so that one does not have regions of paucity on Θ when constructing ϑ_{train} , since neural networks tend to be poor at interpolating over large regions. [Lenzi et al. \(2021\)](#) suggest using likelihood-based estimates to elicit an informative prior from the data: however, this requires likelihood estimation to be feasible in the first place, which is often not the case in applications where neural point estimators are being considered.

Variable sample size. A neural point estimator of the form (6) can be applied to sets of arbitrary size. However, the neural Bayes estimator for replicated data is conditional on the number of replicates used during training, \tilde{m} , and is not necessarily a Bayes estimator for $m \neq \tilde{m}$. Denote a data set comprising m replicates as $\mathbf{Z}^{(m)} \equiv (\mathbf{Z}'_1, \dots, \mathbf{Z}'_m)'$. There are at least two approaches that one could adopt if data sets with varying m are envisaged. First, one could train l neural Bayes estimators for different sample sizes, or groups thereof (e.g., a small-sample estimator and a large-sample estimator). Specifically, for sample-size change-points m_1, m_2, \dots, m_{l-1} , one could construct a piecewise neural Bayes estimator,

$$\hat{\boldsymbol{\theta}}(\mathbf{Z}^{(m)}; \boldsymbol{\gamma}^*) = \begin{cases} \hat{\boldsymbol{\theta}}(\mathbf{Z}^{(m)}; \boldsymbol{\gamma}_{\tilde{m}_1}^*) & m \leq m_1, \\ \hat{\boldsymbol{\theta}}(\mathbf{Z}^{(m)}; \boldsymbol{\gamma}_{\tilde{m}_2}^*) & m_1 < m \leq m_2, \\ \vdots & \\ \hat{\boldsymbol{\theta}}(\mathbf{Z}^{(m)}; \boldsymbol{\gamma}_{\tilde{m}_l}^*) & m > m_{l-1}, \end{cases} \quad (8)$$

where, here, $\boldsymbol{\gamma}^* \equiv (\boldsymbol{\gamma}_{\tilde{m}_1}^*, \dots, \boldsymbol{\gamma}_{\tilde{m}_{l-1}}^*)$, and where $\boldsymbol{\gamma}_{\tilde{m}}^*$ are the neural-network parameters optimised for sample size \tilde{m} chosen so that $\hat{\boldsymbol{\theta}}(\cdot; \boldsymbol{\gamma}_{\tilde{m}}^*)$ is near-optimal over the range of sample sizes in which it is applied. We find that this approach works well in practice, and that it is less computationally burdensome than it first appears when used in conjunction with pre-training (see below). Note that the relative influence of the prior distribution diminishes

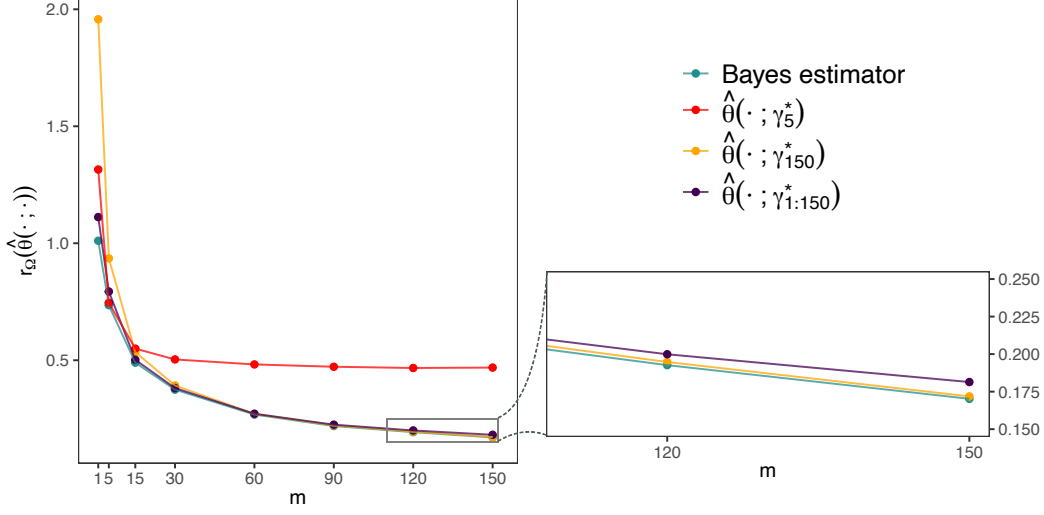


Figure 2: The Bayes risk $r_{\Omega}(\hat{\theta}(\cdot; \cdot))$ plotted against the sample size m , for the theoretical Bayes estimator (green) and several neural Bayes estimators (orange, red, purple) for θ from $N(0, \theta)$ data.

as the sample size increases, so that only a single “large sample” estimator is needed. Alternatively, one could treat the sample size as a random variable, M , with support over a set of positive integers, \mathcal{M} , in which case (1) becomes

$$R(\boldsymbol{\theta}, \hat{\boldsymbol{\theta}}(\cdot; \boldsymbol{\gamma})) \equiv \sum_{m \in \mathcal{M}} P(M = m) \left(\int_{\mathcal{S}^m} L(\boldsymbol{\theta}, \hat{\boldsymbol{\theta}}(\mathbf{Z}^{(m)}; \boldsymbol{\gamma})) p(\mathbf{Z}^{(m)} | \boldsymbol{\theta}) d\mathbf{Z}^{(m)} \right). \quad (9)$$

This approach does not materially alter the workflow, except that one must sample the number of replicates before simulating data for (4). These two approaches can also be combined, so that each sub-estimator in (8) is trained using (9).

To illustrate this dependence on m , we trained neural Bayes estimators with a range of sample sizes, where the inferential target is θ from replicated data generated from a $N(0, \theta)$ distribution. We set the prior distribution over the variance θ to be an InverseGamma(2, 2) distribution. The estimators $\hat{\theta}(\cdot; \boldsymbol{\gamma}_5^*)$ and $\hat{\theta}(\cdot; \boldsymbol{\gamma}_{150}^*)$ were trained with each element of $\mathcal{Z}_{\text{train}}$ corresponding to exactly 5 or 150 replicates, respectively, while the estimator $\hat{\theta}(\cdot; \boldsymbol{\gamma}_{1:150}^*)$ was trained with the elements of $\mathcal{Z}_{\text{train}}$ containing a variable number of replicates and with M in (9) a discrete uniform random variable with support between 1 and 150 inclusive. Figure 2, shows that estimators trained with fixed m are optimal only for that choice of m . On the other hand, the estimator $\hat{\theta}(\cdot; \boldsymbol{\gamma}_{1:150}^*)$ is not optimal for any m , but performs well for all $m \in \{1, \dots, 150\}$. Combining the approaches of (8) and (9) is therefore an effective strategy for constructing a neural Bayes estimator that is near-optimal for all sample sizes.

Pre-training. The parameters of a neural network trained for one task can provide useful initial values for the parameters of another neural network intended for a slightly different task. This is known as pre-training (Goodfellow et al., 2016, Ch. 8). Pre-training is ideal when developing a piecewise neural Bayes estimator (8), whereby one may randomly initialise and train $\hat{\boldsymbol{\theta}}(\cdot; \boldsymbol{\gamma}_{m_1}^*)$, use the parameters $\boldsymbol{\gamma}_{m_1}^*$ to pre-train $\hat{\boldsymbol{\theta}}(\cdot; \boldsymbol{\gamma}_{m_2}^*)$, and so on. Since each

estimator need only account for a larger sample size than that used by its predecessor, scant computational resources are needed to train subsequent estimators. This approach can be useful even when only a single large-sample estimator is needed: doing most of the learning with small, computationally cheap sample sizes can substantially reduce training time when compared to training a single large-sample estimator from scratch. In Section S1 of the Supplementary Material, we empirically illustrate the benefits of this strategy.

“On-the-fly” and “just-in-time” simulation. The ease with which data can be simulated from the models that we are concerned with means that $\mathcal{Z}_{\text{train}}$ can often be simulated periodically during training, a technique that Chan et al. (2018) call “simulation-on-the-fly”. In Section S2 of the Supplementary Material, we conduct an experiment that shows that regularly refreshing $\mathcal{Z}_{\text{train}}$ leads to lower out-of-sample error and to a reduction in overfitting. This strategy therefore facilitates the use of larger, more representationally-powerful networks that are prone to overfitting with fixed $\mathcal{Z}_{\text{train}}$. Refreshing $\mathcal{Z}_{\text{train}}$ also has an additional computational benefit; data can be simulated “just-in-time”, in the sense that they can be simulated from a small batch of ϑ_{train} , used to train the neural point estimator, and then removed from memory. This can reduce pressure on memory resources when $|\vartheta_{\text{train}}|$ is very large.

Chan et al. (2018) also refresh ϑ_{train} , which has similar benefits. Fixing ϑ_{train} , however, allows computationally expensive terms, such as Cholesky factors, to be reused throughout training, which can substantially reduce the training time with some models.

4 Simulation studies

We now conduct several simulation studies that clearly illustrate the utility of neural Bayes estimators for parameter estimation, and their outstanding performance with respect to traditional approximate likelihood-based approaches. In Section 4.1, we outline the general setting. In Section 4.2, we estimate the parameters of a Gaussian process model. In Section 4.3, we estimate the parameters of Schlather’s max-stable model (Schlather, 2002). In Section 4.4, we consider the highly-parameterised conditional extremes model (Wadsworth and Tawn, 2022). We provide simulation details and the likelihood function for each model in Section S3 of the Supplementary Material.

For ease of notation, we omit dependence on the neural-network parameters γ in future references to neural point estimators, so that $\hat{\theta}(\cdot; \gamma)$, $\psi(\cdot; \gamma)$, and $\phi(\cdot; \gamma)$ are written simply as $\hat{\theta}(\cdot)$, $\psi(\cdot)$, and $\phi(\cdot)$, respectively.

4.1 General setting

Across the simulation studies we assume, for ease of exposition, that our processes are spatial. Our spatial domain of interest, \mathcal{D} , is $[0, 16] \times [0, 16]$, and we simulate data on a regular grid with unit-square cells, yielding $16^2 = 256$ observations per spatial field. Convolutional neural networks (CNNs) are a natural choice for regularly-spaced gridded data, and we therefore use a CNN architecture, summarised in Table 1. To implement the neural point estimators, we use the accompanying package **NeuralEstimators** that is written in Julia and which

Table 1: Summary of the neural network architecture used in Section 4. We follow the convention of reporting the dimension of the input array and output array of each layer. A padding of 0 and a stride of 1 are used in each 2D convolution layer. For all layers except the final layer we use a rectified linear unit (ReLU) activation function. For the final layer, we use an identity activation function. Recall that p denotes the number of parameters in the given statistical model.

layer type	input dimension	output dimension	kernel size	parameters
2D convolution	[16, 16, 1]	[7, 7, 64]	10×10	6,464
2D convolution	[7, 7, 64]	[3, 3, 128]	5×5	204,928
2D convolution	[3, 3, 128]	[1, 1, 256]	3×3	295,168
vec(\cdot)	[1, 1, 256]	[256]		0
dense	[256]	[500]		128,500
dense	[500]	[p]		$501p$
total trainable parameters:				$635,060 + 501p$

leverages the package **Flux** (Innes, 2018). We conduct our studies using a workstation with an AMD EPYC 7402 3.00GHz CPU with 52 cores and 128 GB of CPU RAM, and an NVIDIA Quadro RTX 6000 GPU with 24 GB of GPU RAM. All results presented in the remainder of this paper can be generated using reproducible code at [<LinkWillBeInsertedHere>](#).[†]

We consider two neural point estimators which are both based on the architecture given in Table 1. The first estimator, $\hat{\theta}_0(\cdot)$, is the permutation-invariant neural point estimator considered by Gerber and Nychka (2021) which is an average of one-at-a-time estimators. The second estimator, $\hat{\theta}_{\text{DS}}(\cdot)$, is the piecewise neural point estimator (8), where each sub-estimator employs the representation (5) with $\psi(\cdot)$ and $\phi(\cdot)$ constructed using the first four and last two rows of Table 1, respectively. Five sub-estimators are used, with training sample sizes $\tilde{m}_1 = 1$, $\tilde{m}_2 = 10$, $\tilde{m}_3 = 35$, $\tilde{m}_4 = 75$, and $\tilde{m}_5 = 150$.

We assume that the parameters $\theta_1, \dots, \theta_p$ are a priori independent and uniformly distributed on an interval that is parameter dependent. We train the neural point estimators under the absolute-error loss. We set $|\vartheta_{\text{train}}| = 10,000$ and $|\vartheta_{\text{val}}| = 2,000$, and we keep these sets fixed during training. We construct $\mathcal{Z}_{\text{train}}$ and \mathcal{Z}_{val} by simulating 10 sets of m model realisations for each element of ϑ_{train} and ϑ_{val} , respectively. During training, we fix \mathcal{Z}_{val} but simulate $\mathcal{Z}_{\text{train}}$ on-the-fly; hence, in this paper, we define an “epoch” as a pass through $\mathcal{Z}_{\text{train}}$ when doing stochastic gradient descent, before it is refreshed. We cease training when the risk evaluated using ϑ_{val} and \mathcal{Z}_{val} has not decreased in 5 consecutive epochs.

We compare the neural point estimators to the maximum a posteriori (MAP) estimator,

$$\hat{\theta}_{\text{MAP}}(\mathbf{Z}) \equiv \arg \max_{\theta \in \Theta} \sum_{i=1}^m \ell(\theta; \mathbf{Z}_i) + \log p(\theta), \quad (10)$$

where $\ell(\theta; \cdot)$ is the log-likelihood function for a single replicate. We solve (10) using the true parameters as initial values for the Nelder-Mead algorithm (Nelder and Mead, 1965). We

[†]Reproducible code will be made freely available on [GitHub](#) after manuscript acceptance with a journal. The code leverages functionality from a package that will also be made available on [GitHub](#) upon acceptance. An anonymous version of the online documentation with example usage is provided as supplementary material (please open `index.html` in any web browser).

advantage the competitor MAP estimator, which optimises the risk with respect to the 0-1 loss, by assessing all estimators with respect to the 0-1 loss, with $|\vartheta_{\text{test}}| = 500$.

4.2 Gaussian process model

Spatial statistics is concerned with modelling data that are collected across space; reference texts include [Cressie \(1993\)](#), [Banerjee et al. \(2004\)](#), and [Diggle and Ribeiro \(2007\)](#). Here, we consider a classical spatial model, the linear Gaussian-Gaussian model,

$$Z_{ij} = Y_i(\mathbf{s}_j) + \epsilon_{ij}, \quad i = 1, \dots, m, \quad j = 1, \dots, n, \quad (11)$$

where $\mathbf{Z}_i \equiv (Z_{i1}, \dots, Z_{in})'$ are data observed at locations $\{\mathbf{s}_1, \dots, \mathbf{s}_n\}$ on a spatial domain \mathcal{D} , $\{Y_i(\cdot)\}$ are i.i.d. spatially-correlated mean-zero Gaussian processes, and $\epsilon_{ij} \sim N(0, \sigma_\epsilon^2)$ is Gaussian white noise. The covariance function, $C(\mathbf{s}, \mathbf{u}) \equiv \text{cov}(Y_i(\mathbf{s}), Y_i(\mathbf{u}))$, for $\mathbf{s}, \mathbf{u} \in \mathcal{D}$ and $i = 1, \dots, m$, is the primary mechanism for capturing spatial dependence. Note that, since $\{Y_i(\cdot)\}$ are i.i.d., we have that $\text{cov}(Y_i(\mathbf{s}), Y_{i'}(\mathbf{u})) = 0$ for all $i \neq i'$ and $\mathbf{s}, \mathbf{u} \in \mathcal{D}$. Here, we use the popular isotropic Matérn covariance function,

$$C(\mathbf{s}, \mathbf{u}) = \sigma^2 \frac{2^{1-\nu}}{\Gamma(\nu)} \left(\frac{\|\mathbf{s} - \mathbf{u}\|}{\rho} \right)^\nu K_\nu \left(\frac{\|\mathbf{s} - \mathbf{u}\|}{\rho} \right), \quad (12)$$

where σ^2 is the marginal variance, $\Gamma(\cdot)$ the gamma function, $K_\nu(\cdot)$ is the Bessel function of the second kind of order ν , and $\rho > 0$ and $\nu > 0$ are the range and smoothness parameters, respectively. We follow [Gerber and Nychka \(2021\)](#) and fix $\sigma^2 = 1$. This leaves three unknown parameters that need to be estimated: $\boldsymbol{\theta} \equiv (\sigma_\epsilon, \rho, \nu)'$.

Fixing ν simplifies the estimation task, since the remaining parameters are usually well-identified from just a single replicate; we consider this model, which was also considered by [Gerber and Nychka \(2021\)](#), in Section S4 of the Supplementary Material. Here, we consider the case where all three parameters are unknown. Inference in this case is more challenging since ρ and ν are only weakly identifiable from a single replicate ([Zhang, 2004](#)), but inference on ν is important since it controls the differentiability of the process ([Stein, 1999](#), Ch. 2).

We use the priors $\sigma_\epsilon \sim \text{Unif}(0.1, 1)$, $\rho \sim \text{Unif}(2, 10)$, and $\nu \sim \text{Unif}(0.5, 3)$. The total training time for $\hat{\boldsymbol{\theta}}_0(\cdot)$ is 15 minutes. The training time for $\hat{\boldsymbol{\theta}}_{\text{DS}}(\cdot)$, despite it consisting of several sub-estimators and being trained with large sample sizes, is only slightly more, at 33 minutes, due to the pre-training strategy discussed in Section 3. This modest increase in training time is a small cost when accounting for the improvement in statistical efficiency, as shown in Figure 3. Clearly, $\hat{\boldsymbol{\theta}}_{\text{DS}}(\cdot)$ substantially improves over $\hat{\boldsymbol{\theta}}_0(\cdot)$, and performs similarly well to the optimal MAP estimator. When estimating ϑ_{test} , the neural point estimators take 0.1 and 2 seconds when $m = 1$ and $m = 150$, respectively, while the MAP estimator takes between 600 and 800 seconds.

Next, we compare the empirical joint distributions of the estimators for a single member of ϑ_{test} . Figure 4 shows the true parameters (red cross) and corresponding estimates obtained by applying each estimator to 100 sets of $m = 150$ independent model realisations. The MAP estimator and $\hat{\boldsymbol{\theta}}_{\text{DS}}(\cdot)$ are both approximately unbiased, and both are able to capture the correlations expected when using the parameterisation (12); both are clearly much better than $\hat{\boldsymbol{\theta}}_0(\cdot)$. Empirical joint distributions for additional parameters in ϑ_{test} are shown in

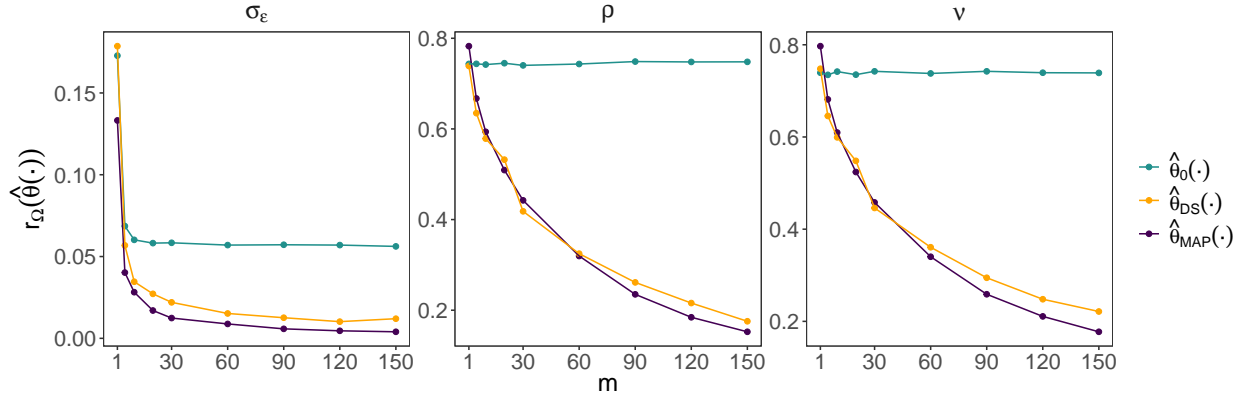


Figure 3: The risk with respect to the 0–1 loss against the number of replicates, m , available for each parameter vector in ϑ_{test} , for the estimators considered in Section 4.2. The estimators $\hat{\theta}_0(\cdot)$, $\hat{\theta}_{\text{DS}}(\cdot)$, and the MAP estimator are shown in green, orange, and purple, respectively.

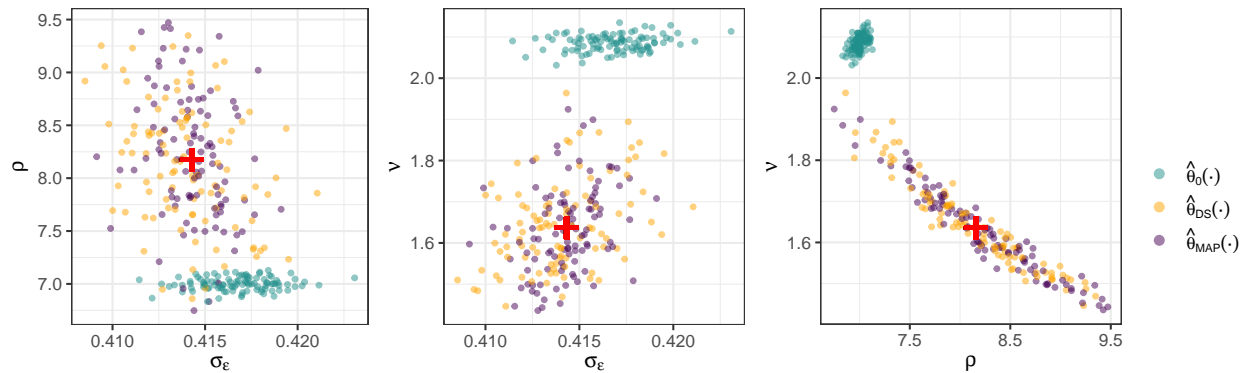


Figure 4: The empirical joint distribution of the estimators considered in Section 4.2 for a single parameter vector in ϑ_{test} . The true parameters are shown in red, while estimates from $\hat{\theta}_0(\cdot)$, $\hat{\theta}_{\text{DS}}(\cdot)$, and the MAP estimator are shown in green, orange, and purple, respectively. Each estimate was obtained from a simulated data set of size $m = 150$.

Figure S10 of the Supplementary Material, and lead to similar conclusions to those drawn here. Overall, these results show that $\hat{\theta}_{\text{DS}}(\cdot)$ is a substantial improvement over the prior art, $\hat{\theta}_0(\cdot)$, and that $\hat{\theta}_{\text{DS}}(\cdot)$ is competitive with the likelihood-based estimator for this model.

4.3 Schlather’s max-stable model

We now consider models used for spatial extremes, useful reviews for which are given by Davison et al. (2019) and Huser and Wadsworth (2022). Max-stable processes are the cornerstone of spatial extreme-value analysis, being the only possible non-degenerate limits of properly renormalized pointwise block maxima of i.i.d. random fields. However, their practical use has been severely hampered due to the computational bottleneck in evaluating their likelihood function. They are thus natural models to consider in our experiments, and we here start with a fairly simple max-stable model with only two parameters, also considered by Lenzi et al. (2021). Specifically, we consider Schlather’s max-stable model (Schlather,

2002), given by

$$Z_{ij} = \bigvee_{k \in \mathbb{N}} \zeta_{ik} \max\{0, Y_{ik}(\mathbf{s}_j)\}, \quad i = 1, \dots, m, \quad j = 1, \dots, n, \quad (13)$$

where \bigvee denotes the maximum over the indexed terms, $\mathbf{Z}_i \equiv (Z_{i1}, \dots, Z_{in})'$ are observed at locations $\{\mathbf{s}_1, \dots, \mathbf{s}_n\} \subset \mathcal{D}$, $\{\zeta_{ik} : k \in \mathbb{N}\}$ for $i = 1, \dots, m$ are i.i.d. Poisson point processes on $(0, \infty)$ with intensity measure $d\Lambda(\zeta) = \zeta^{-2}d\zeta$, and $\{Y_{ik}(\cdot) : i = 1, \dots, m, k \in \mathbb{N}\}$ are i.i.d. mean-zero Gaussian processes scaled so that $\mathbb{E}[\max\{0, Y_{ik}(\cdot)\}] = 1$. Here, we model each $Y_{ik}(\cdot)$ using the Matérn covariance function (12), with $\sigma^2 = 1$. Hence, $\boldsymbol{\theta} \equiv (\rho, \nu)'$.

We use the same uniform priors for ρ and ν as used in Section 4.2. Realisations from the present model, here expressed on unit Fréchet margins, tend to have highly varying magnitudes (see Figure S11 of the Supplementary Material), and we reduce this variability by log-transforming our data to the unit Gumbel scale. The total training time for $\hat{\boldsymbol{\theta}}_0(\cdot)$ and $\hat{\boldsymbol{\theta}}_{\text{DS}}(\cdot)$ is 14 and 66 minutes, respectively.

As in Section 4.2, we assess the neural point estimators by comparing them to a likelihood-based estimator. For Schlather’s model (and other max-stable models in general), the full likelihood function is computationally intractable, since it involves a summation over the set of all possible partitions of the replicates (see, e.g., Padoan et al., 2010, Huser et al., 2019, and the references therein). A popular substitute is the pairwise likelihood (PL) function, a composite likelihood formed by considering only pairs of observations; specifically, the pairwise log-likelihood function for the i th replicate is

$$\ell_{\text{P}}(\boldsymbol{\theta}; \mathbf{Z}_i) \equiv \sum_{j=1}^{n-1} \sum_{j'=j+1}^n \log f(Z_{ij}, Z_{ij'}; \boldsymbol{\theta}), \quad (14)$$

where $f(\cdot, \cdot; \boldsymbol{\theta})$ denotes the bivariate probability density function for pairs in \mathbf{Z}_i which, for Schlather’s model, is given in Section S3.2 of the Supplementary Material. Under mild regularity conditions, the maximum PL estimator, obtained by maximising $\sum_{i=1}^m \ell_{\text{P}}(\boldsymbol{\theta}; \mathbf{Z}_i)$, has similar asymptotic properties to the ML estimator (i.e., consistency, asymptotic normality), since the pairwise log-likelihood function is a linear combination of unbiased estimating equations. Hence, in this subsection, we compare the neural point estimators to the pairwise MAP (PMAP) estimator, that is, (10) with the full log-likelihood function replaced by (14). Often, both computational and statistical efficiency can be drastically improved by using only a subset of pairs that are within a fixed cut-off distance, d (see, e.g., Bevilacqua et al., 2012, Sang and Genton, 2012). A line-search for d (see Figure S12 of the Supplementary Material for details) shows that, here, $d = 3$ units provides good results.

The left and centre panels of Figure 5 show the estimators’ risk against the number of independent replicates available for each member of ϑ_{test} . For small samples, both neural point estimators improve over the PMAP estimator. For moderate-to-large samples, $\hat{\boldsymbol{\theta}}_0(\cdot)$ hits a performance plateau, while $\hat{\boldsymbol{\theta}}_{\text{DS}}(\cdot)$ continues to substantially outperform the PMAP estimator. The run time for the neural point estimators to estimate all parameters in ϑ_{test} scales linearly between 0.1 and 1.5 seconds for $m = 1$ and $m = 150$, respectively, while the PMAP estimator takes between 750 and 1900 seconds. The right panel of Figure 5 shows the empirical joint distribution of the estimators for a single parameter vector in ϑ_{test} , where each

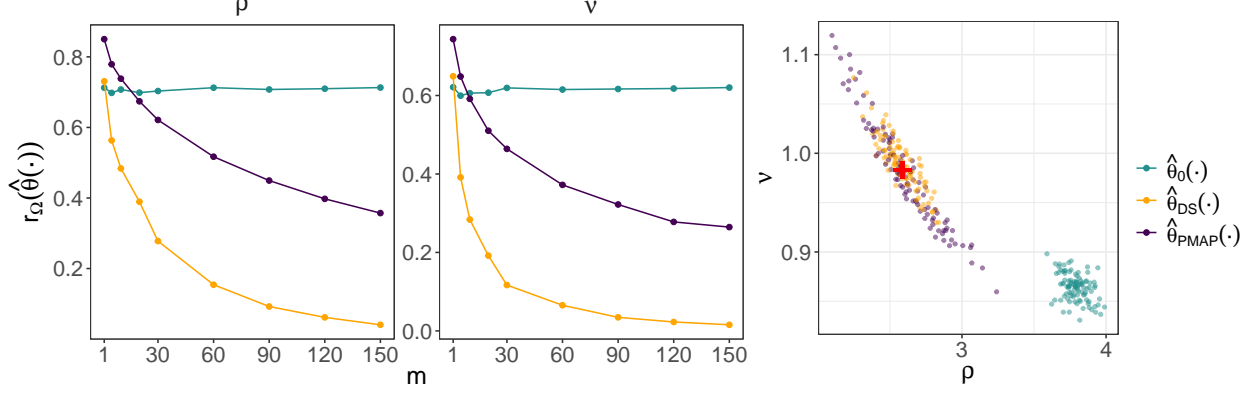


Figure 5: Diagnostic plots for the simulation study of Section 4.3. (Left and centre) The risk with respect to the 0–1 loss against the number of replicates, m , available for each parameter vector in ϑ_{test} . (Right) True parameters (red) and corresponding estimates, each of which was obtained using a simulated data set of size $m = 150$. In all panels, $\hat{\theta}_0(\cdot)$, $\hat{\theta}_{\text{DS}}(\cdot)$, and the pairwise MAP estimator are shown in green, orange, and purple, respectively.

estimate was obtained from $m = 150$ replicates. Again, $\hat{\theta}_0(\cdot)$ is strongly biased, while the PMAP estimator is unbiased but is less efficient than $\hat{\theta}_{\text{DS}}(\cdot)$. Empirical joint distributions for additional parameters in ϑ_{test} are shown in Figure S13 of the Supplementary Material, and lead to similar conclusions to those drawn here. Overall, the proposed estimator, $\hat{\theta}_{\text{DS}}(\cdot)$, is superior to the likelihood-based technique for Schlather’s max-stable model.

4.4 Spatial conditional extremes model

While max-stable processes are asymptotically justified for modelling spatial extremes defined as block maxima, they have strong limitations in practice (Huser and Wadsworth, 2022). Beyond the intractability of their likelihood function in high dimensions, max-stable models have an overly rigid dependence structure, and in particular cannot capture a property known as asymptotic tail independence. Therefore, different model constructions, justified by alternative asymptotic conditions, have been recently proposed to circumvent the restrictions imposed by max-stability. In particular, the spatial conditional extremes model, first introduced by Wadsworth and Tawn (2022) as a spatial extension of the multivariate Heffernan and Tawn (2004) model, and subsequently studied and used in applications by, for example, Simpson et al. (2021) and Richards et al. (2021), is especially appealing. This model has a flexible dependence structure capturing both asymptotic tail dependence and independence (Wadsworth and Tawn, 2022) and leads to likelihood-based inference amenable to higher dimensions. Nevertheless, making inference remains challenging because this model is complex and is typically highly parameterised. Here, we consider a version of the spatial conditional extremes model that involves eight dependence parameters in total.

Our formulation of the model is similar to that originally proposed by Wadsworth and Tawn (2022). Specifically, we model the process conditional on it exceeding a threshold, u , at a conditioning site, $\mathbf{s}_0 \in \mathcal{D}$, as

$$Z_{ij} \mid Z_{i0} > u \stackrel{\text{d}}{=} a(\mathbf{h}_j, Z_{i0}) + b(\mathbf{h}_j, Z_{i0})Y_i(\mathbf{s}_j), \quad i = 1, \dots, m, \quad j = 1, \dots, n, \quad (15)$$

where ‘ $\stackrel{d}{=}$ ’ denotes equality in distribution, Z_{i0} is the datum at \mathbf{s}_0 , $\mathbf{h}_j \equiv \mathbf{s}_j - \mathbf{s}_0$, and $Z_{i0} - u \mid Z_{i0} > u$ is a unit exponential random variable that is independent of the residual process, $Y_i(\cdot)$, which we describe below. We model $a(\cdot, \cdot)$ and $b(\cdot, \cdot)$ using parametric forms proposed by [Wadsworth and Tawn \(2022\)](#),

$$\begin{aligned} a(\mathbf{h}, z) &= z \exp\{-(\|\mathbf{h}\|/\lambda)^\kappa\}, \quad \lambda > 0, \kappa > 0, \\ b(\mathbf{h}, z) &= 1 + a(\mathbf{h}, z)^\beta, \quad \beta > 0, \end{aligned}$$

where $\mathbf{h} \equiv \mathbf{s} - \mathbf{s}_0$ for $\mathbf{s} \in \mathcal{D}$ and $z \in \mathbb{R}$. We construct the residual process, $Y_i(\cdot)$, by first defining $\tilde{Y}_i^{(0)}(\cdot) \equiv \tilde{Y}_i(\cdot) - \tilde{Y}_i(\mathbf{s}_0)$, with $\tilde{Y}_i(\cdot)$ a mean-zero Gaussian process with Matérn covariance function and unit marginal variance, and then marginally transforming it to the scale of a delta-Laplace (generalised Gaussian) distribution ([Subbotin, 1923](#)) which, for $y \in \mathbb{R}$ and parameters $\mu \in \mathbb{R}, \tau > 0, \delta > 0$, has density function

$$f(y) = \frac{\delta}{2\tau\Gamma(1/\delta)} \exp\left(-\left|\frac{y - \mu}{\tau}\right|^\delta\right).$$

We model δ as decaying from 2 to 1 as the distance to \mathbf{s}_0 increases; specifically,

$$\delta(\mathbf{h}) = 1 + \exp\left\{-\left(\|\mathbf{h}\|/\delta_1\right)^2\right\}, \quad \delta_1 > 0. \quad (16)$$

We defer to [Wadsworth and Tawn \(2022\)](#) for model justification and interpretation of model parameters. The threshold u is a modelling decision made to ensure that the data are sufficiently extreme and that, in a real-data setting, we have sufficiently many fields available for estimation: here, we set u to the 0.975 quantile of the unit-Laplace distribution. For simplicity, we consider \mathbf{s}_0 fixed and in the centre of \mathcal{D} .

We again use uniform priors, with $\kappa \sim \text{Unif}(1, 2)$, $\lambda \sim \text{Unif}(2, 5)$, $\beta \sim \text{Unif}(0.05, 1)$, $\mu \sim \text{Unif}(-0.5, 0.5)$, $\tau \sim \text{Unif}(0.3, 0.9)$, $\delta_1 \sim \text{Unif}(1.3, 3)$, and with the same priors for ρ and ν as used in the preceding sections. We use the cube-root function as a variance-stabilising transformation. The training time for $\hat{\boldsymbol{\theta}}_0(\cdot)$ and $\hat{\boldsymbol{\theta}}_{\text{DS}}(\cdot)$ is 22 and 43 minutes, respectively.

Figure 6 shows the risk against the number of replicates, and shows that $\hat{\boldsymbol{\theta}}_{\text{DS}}(\cdot)$ clearly outperforms $\hat{\boldsymbol{\theta}}_0(\cdot)$. Figure 7 shows the empirical joint distribution of the estimators for a single member of $\mathcal{V}_{\text{test}}$ (lower triangle) and simulations from the corresponding model (upper triangle). The estimator $\hat{\boldsymbol{\theta}}_{\text{DS}}(\cdot)$ is approximately unbiased for all parameters and captures the expected negative correlation between ρ and ν . Overall, the estimator $\hat{\boldsymbol{\theta}}_{\text{DS}}(\cdot)$ is clearly suitable for this highly parameterised model, which is an important result for this framework.

5 Application to Red Sea surface temperature

We now apply our methodology to the analysis of sea-surface temperature data in the Red Sea, which have also been analysed by [Hazra and Huser \(2021\)](#), [Simpson and Wadsworth \(2021\)](#), and [Simpson et al. \(2021\)](#), among others, and have been the subject of a competition in the prediction of extreme events ([Huser, 2021](#)). The data set we analyse comprises daily observations from the years 1985 to 2015, for 16703 regularly-spaced locations across the Red Sea; see [Donlon et al. \(2012\)](#) for further details. Following [Simpson et al. \(2021\)](#), we focus

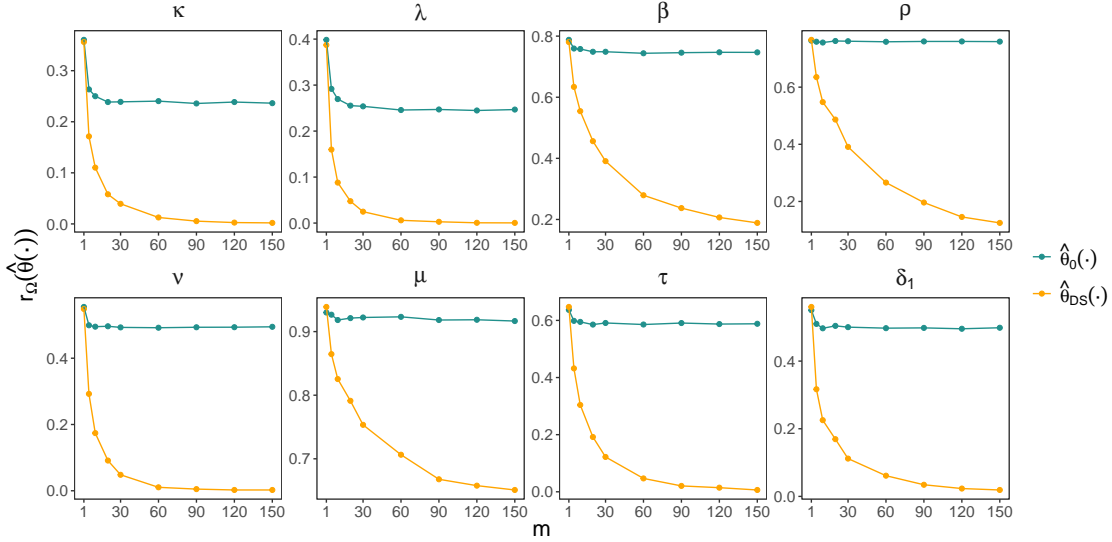


Figure 6: The risk with respect to the 0–1 loss against the number of replicates, m , available for each parameter vector in ϑ_{test} , for the estimators considered in Section 4.4. The estimators $\hat{\theta}_0(\cdot)$ and $\hat{\theta}_{\text{DS}}(\cdot)$ are shown in green and orange, respectively.

on a southern portion of the Red Sea, consider only the summer months to approximately eliminate the effects of seasonality, and retain only every third longitude and latitude value; this yields a data set with 678 unique spatial locations that are regularly-spaced but contained within an irregularly-shaped spatial domain, \mathcal{D} . To account for \mathcal{D} lying away from the equator, we follow [Simpson et al. \(2021\)](#) in scaling the longitude and latitude so that each unit distance in the spatial domain corresponds to approximately 100 km.

To model these data, we use the spatial conditional extremes model described in Section 4.4. We transform our data to the Laplace scale and set the threshold, u in (15), to the 95th percentile of the transformed data. This yields 141 spatial fields for which the transformed datum at the conditioning site, \mathbf{s}_0 , here chosen to lie in the centre of \mathcal{D} as in [Simpson et al. \(2021\)](#), is greater than u ; a randomly-selected sample of these extreme fields are shown in the top row of Figure 8.

The irregular shape of \mathcal{D} means that CNNs are not directly applicable. We use the standard technique of padding empty regions with zeros, so that each field is a 29×37 rectangular array consisting of a data region and a padded region, as shown in Figure S14 of the Supplementary Material. We use the same prior distributions as in Section 4.4, but with those associated with range parameters scaled appropriately. Our architecture is the same as that given in Table 1, but with an additional convolutional layer with a kernel size of 14×22 , which transforms the input array to dimension 16×16 . We validate our neural Bayes estimator using the approach taken in Section 4 (figures omitted for brevity).

Once training is complete, we can compute parameter estimates for the observed data. Table 2 gives estimates and 95% confidence intervals for the estimates. These confidence intervals are obtained using the non-parametric bootstrap procedure described in Section S5 of the Supplementary Material, which accounts for temporal dependence between the spatial fields. Estimation from a single set of 141 fields takes only 0.008 seconds, meaning that boot-

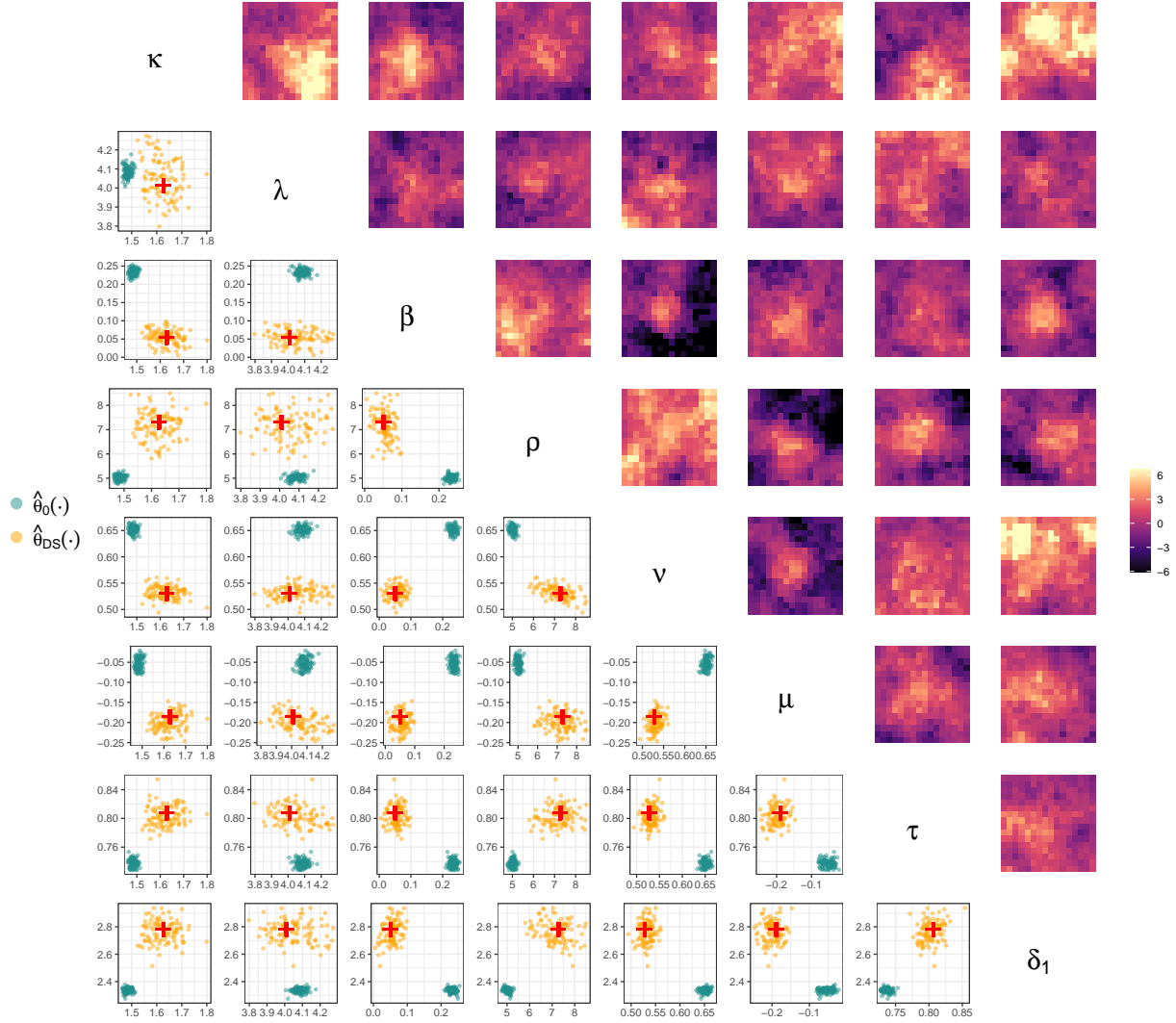


Figure 7: (Lower triangle) The empirical joint distribution of the estimators considered in Section 4.4 for a single parameter vector in $\mathcal{V}_{\text{test}}$. The true parameters are shown in red, while estimates from $\hat{\theta}_0(\cdot)$ and $\hat{\theta}_{DS}(\cdot)$ are shown in green and orange, respectively. Each estimate was obtained from a simulated data set of size $m = 150$. (Upper triangle) Simulations from the model.

strap confidence intervals can be obtained very quickly. This is clearly an advantage of using neural point estimators, as opposed to likelihood-based techniques for which uncertainty assessment in complex models is usually a computational burden.

We use two diagnostic plots to validate the fitted model. First, Figure 8 shows that simulations from the fitted model display properties that are, on the whole, qualitatively similar to the observed data. Next, following [Simpson et al. \(2021\)](#), we separate \mathcal{D} into 17 non-overlapping regions, which are shown in the left panel of Figure 9. Given that the transformed datum at \mathbf{s}_0 exceeds u , we estimate (and quantify the uncertainty in) the proportion of locations in each region that also exceed u , using both model-based and empirical methods. These are shown in the right panel of Figure 9, and indicate overall agreement between the model and the observed data, with some minor lack of fit at very short distances. The

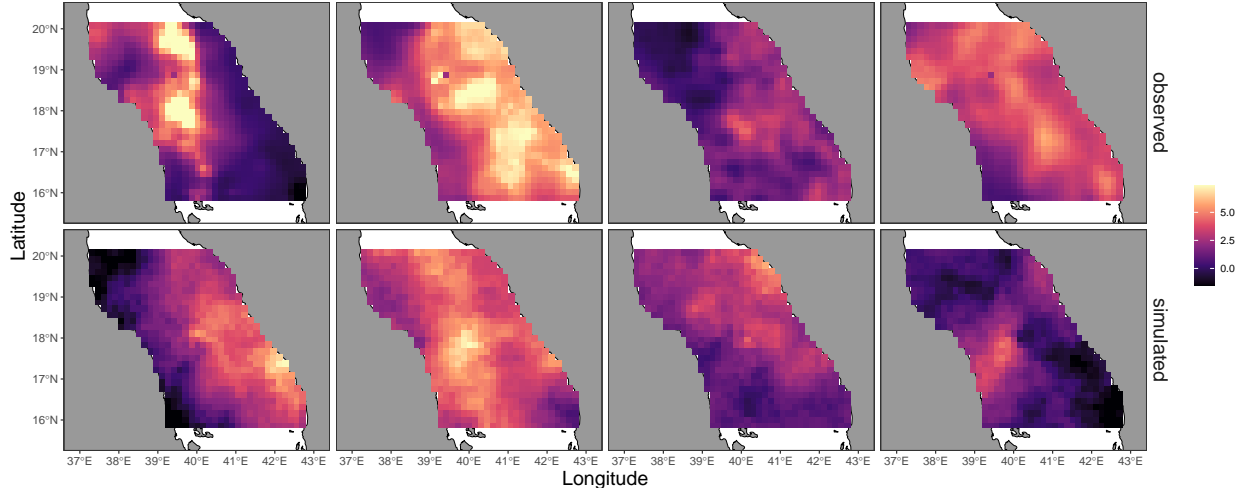


Figure 8: (Top row) Randomly-selected extreme fields from the Red Sea data set considered in Section 5, where $Z(\mathbf{s}_0) > u$. (Bottom row) Simulations from the fitted model. The data are overlaid on a map where the grey areas correspond to land (Sudan and Eritrea to the West, Saudi Arabia to the East) and the white areas correspond to sea.

Table 2: Parameter estimates and 95% bootstrap confidence intervals (provided via the 2.5 and 97.5 percentiles of the bootstrap distribution) for the Red Sea data set of Section 5.

	κ	λ	β	ρ	ν	μ	τ	δ_1
Estimate	1.00	2.74	0.24	1.34	0.78	0.09	0.56	1.22
2.5%	0.88	2.13	0.14	0.95	0.70	0.04	0.49	0.91
97.5%	1.19	3.79	0.40	1.85	0.87	0.14	0.65	1.63

empirical estimates are not monotonically decreasing as a function of distance; this could be due to complex spatial dynamics or non-stationarity in the data, or it could simply be an artefact of sampling variability. In either case, the fit is reasonable, which suggests that our neural Bayes estimator has provided reasonable parameter estimates for this data set.

6 Conclusion

Neural point estimators are a class of amortised likelihood-free estimators that are grounded in classical estimation theory. Their connection to Bayes estimators, so often used in statistical applications, is often under-appreciated, and we hope that this paper increases the awareness and adoption of this powerful tool by statisticians. We have also proposed a principled way to construct neural point estimators for replicated data via the DeepSets architecture. Using these estimators, we jointly estimated the range and smoothness parameters in a Gaussian process model and in Schlather’s max-stable model, and we made inference with the highly-parameterised spatial conditional extremes model. These estimators were implemented with just a few lines of code, thanks to the package **NeuralEstimators**, which is released with this paper and is available at [<LinkWillBeInsertedHere>](#).

There are many avenues for future research. In this work, we have illustrated neural

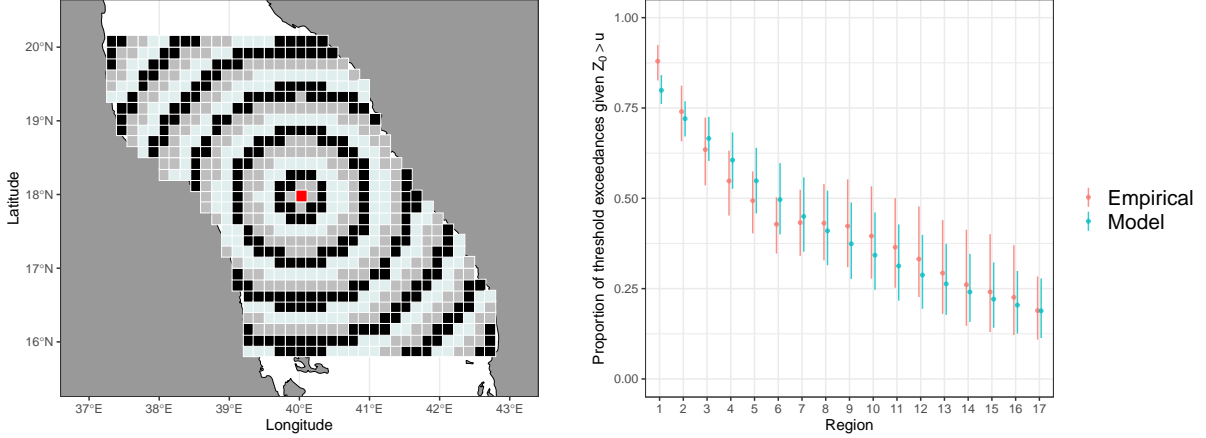


Figure 9: (Left) The spatial domain of interest for the Red Sea study of Section 5, with the conditioning site, s_0 , shown in red, and the remaining locations separated into 17 regions; the region labels begin at 1 in the centre of the domain and increase with distance from the centre. (Right) The estimated proportion of locations for which the process exceeds u given that it is exceeded at s_0 (points) and corresponding 95% confidence intervals (vertical segments) using model-simulated and empirical bootstrap data sets.

point estimation with spatial data observed over a regular grid. Optimal inference from irregular spatial data is an important problem, and one that we consider briefly with dense neural networks in Section S6 of the Supplementary Material: future work may see the use of graphical convolutional neural networks (see, e.g., Wu et al., 2021), which generalise the convolution operation to irregular data. Ways to incorporate covariate information also need to be explored. A possible criticism of neural point estimators is that they are not robust to model misspecification since neural networks are, generally, poor extrapolators. However, we did not find this to be the case in our work. In Section S7 of the Supplementary Material, we provide some empirical evidence that neural point estimators can extrapolate beyond the sample space of the assumed model reasonably well, but further research on this topic is needed. Finally, neural point estimators of the form (6) are ideally placed for online learning problems; investigating their potential in this context is the subject of future work.

Acknowledgements

Matthew Sainsbury-Dale’s and Andrew Zammit-Mangion’s research was supported by an Australian Research Council (ARC) Discovery Early Career Research Award, DE180100203. Matthew Sainsbury-Dale’s research was also supported by an Australian Government Research Training Program Scholarship and a 2022 Statistical Society of Australia (SSA) top-up scholarship. Raphaël Huser was partially supported by the King Abdullah University of Science and Technology (KAUST) Office of Sponsored Research (OSR) under Award No. OSR-CRG2020-4394. The authors would like to acknowledge Johan Barthelemy, NVIDIA, SMART Infrastructure Facility of the University of Wollongong, as well as a 2021 Major Equipment Grant from the University of Wollongong’s University Research Committee, that together have provided access to extensive GPU computing resources. The authors would

also like to thank Yi Cao for technical support. Thanks also go to Emma Simpson, Jennifer Wadsworth, and Thomas Opitz for providing access to the Red Sea data set, and code for preprocessing it. The authors are also grateful to Noel Cressie and Jonathan Rougier for providing helpful comments on the manuscript.

A Permutation-invariance of Bayes estimators

Let $\mathcal{P} \equiv \{P_{\boldsymbol{\theta}} : \boldsymbol{\theta} \in \Theta\}$ denote a class of distributions parameterised by $\boldsymbol{\theta}$, and let $\Omega(\cdot)$ denote a prior measure over $\boldsymbol{\theta}$. For a strictly convex loss function $L(\cdot, \cdot)$, the Bayes estimator $\hat{\boldsymbol{\theta}}^*(\cdot)$ for replicated data (i.e., data that are conditionally independent given $\boldsymbol{\theta}$) is unique and permutation invariant with probability 1 provided that

- (i) the Bayes risk of $\hat{\boldsymbol{\theta}}^*(\cdot)$ is finite, and
- (ii) the distribution $P_{\boldsymbol{\theta}}(\cdot)$ is absolutely continuous with respect to the marginal distribution $\int P_{\boldsymbol{\theta}}(\cdot) d\Omega(\boldsymbol{\theta})$.

Proof. The proposition is a straightforward extension of [Lehmann and Casella \(1998, Ch. 4, Cor. 1.4\)](#) for the special case where the posterior distribution is invariant to the ordering of the data, as is the case with conditionally-independent replicates. Here, for ease of exposition, we give the proof for the case where the prior distribution admits a density $p(\boldsymbol{\theta})$ and where the distribution of the data under $P_{\boldsymbol{\theta}}(\cdot)$ admits a density $p(\cdot | \boldsymbol{\theta})$ with respect to Lebesgue measure. This proof is based on the following two properties:

- (a) (Permutation invariance) The posterior density for $\boldsymbol{\theta}$ is given by

$$p(\boldsymbol{\theta} | \mathbf{Z}) = \frac{p(\boldsymbol{\theta}) \prod_{i=1}^m p(\mathbf{Z}_i | \boldsymbol{\theta})}{\int_{\Theta} p(\boldsymbol{\theta}) \prod_{i=1}^m p(\mathbf{Z}_i | \boldsymbol{\theta}) d\boldsymbol{\theta}} = p(\boldsymbol{\theta} | \mathbf{Z}_{\pi}), \quad (17)$$

where $\mathbf{Z}_{\pi} \equiv \pi(\mathbf{Z}) = (\mathbf{Z}'_{\pi(1)}, \dots, \mathbf{Z}'_{\pi(m)})'$ is a permutation under $\pi(\cdot)$ of the conditionally independent replicates in $\mathbf{Z} \equiv (\mathbf{Z}'_1, \dots, \mathbf{Z}'_m)'$.

- (b) (Minimisation of posterior expected loss) For a given \mathbf{Z} , a Bayes estimator $\hat{\boldsymbol{\theta}}^*(\mathbf{Z})$ is a minimiser over $\hat{\boldsymbol{\theta}}(\mathbf{Z})$ of

$$\int_{\Theta} L(\boldsymbol{\theta}, \hat{\boldsymbol{\theta}}(\mathbf{Z})) p(\boldsymbol{\theta} | \mathbf{Z}) d\boldsymbol{\theta}. \quad (18)$$

Now, by optimality of the Bayes estimator, we have that

$$\begin{aligned} \int_{\Theta} L(\boldsymbol{\theta}, \hat{\boldsymbol{\theta}}^*(\mathbf{Z})) p(\boldsymbol{\theta} | \mathbf{Z}) d\boldsymbol{\theta} &\leq \int_{\Theta} L(\boldsymbol{\theta}, \hat{\boldsymbol{\theta}}^* \circ \pi(\mathbf{Z})) p(\boldsymbol{\theta} | \mathbf{Z}) d\boldsymbol{\theta} \\ &= \int_{\Theta} L(\boldsymbol{\theta}, \hat{\boldsymbol{\theta}}^*(\mathbf{Z}_{\pi})) p(\boldsymbol{\theta} | \mathbf{Z}) d\boldsymbol{\theta}, \end{aligned}$$

since $\hat{\boldsymbol{\theta}}^* \circ \pi(\cdot)$ is a different (potentially non-Bayes) estimator formed by the composition of the Bayes estimator and a permutation function. Similarly, for observations \mathbf{Z}_{π} , we have

that

$$\begin{aligned}
\int_{\Theta} L(\boldsymbol{\theta}, \hat{\boldsymbol{\theta}}^*(\mathbf{Z}_{\pi})) p(\boldsymbol{\theta} \mid \mathbf{Z}_{\pi}) d\boldsymbol{\theta} &= \int_{\Theta} L(\boldsymbol{\theta}, \hat{\boldsymbol{\theta}}^*(\mathbf{Z}_{\pi})) p(\boldsymbol{\theta} \mid \mathbf{Z}) d\boldsymbol{\theta} \quad (\text{by (17)}) \\
&\leq \int_{\Theta} L(\boldsymbol{\theta}, \hat{\boldsymbol{\theta}}^* \circ \pi^{-1}(\mathbf{Z}_{\pi})) p(\boldsymbol{\theta} \mid \mathbf{Z}) d\boldsymbol{\theta} \\
&= \int_{\Theta} L(\boldsymbol{\theta}, \hat{\boldsymbol{\theta}}^*(\mathbf{Z})) p(\boldsymbol{\theta} \mid \mathbf{Z}) d\boldsymbol{\theta},
\end{aligned}$$

and therefore

$$\begin{aligned}
\int_{\Theta} L(\boldsymbol{\theta}, \hat{\boldsymbol{\theta}}^*(\mathbf{Z})) p(\boldsymbol{\theta} \mid \mathbf{Z}) d\boldsymbol{\theta} &= \int_{\Theta} L(\boldsymbol{\theta}, \hat{\boldsymbol{\theta}}^*(\mathbf{Z}_{\pi})) p(\boldsymbol{\theta} \mid \mathbf{Z}) d\boldsymbol{\theta} \\
&= \int_{\Theta} L(\boldsymbol{\theta}, \hat{\boldsymbol{\theta}}^* \circ \pi(\mathbf{Z})) p(\boldsymbol{\theta} \mid \mathbf{Z}) d\boldsymbol{\theta}.
\end{aligned}$$

Since $L(\cdot, \cdot)$ is strictly convex, if conditions (i) and (ii) hold, the Bayes estimator is unique with probability 1 (Lehmann and Casella, 1998, Ch. 4, Cor. 1.4), and

$$\hat{\boldsymbol{\theta}}^*(\mathbf{Z}) = \hat{\boldsymbol{\theta}}^* \circ \pi(\mathbf{Z}), \quad (19)$$

with probability 1 for any \mathbf{Z} and permutation function $\pi(\cdot)$. \square

References

- Banerjee, S., Carlin, B. P., and Gelfand, A. E. (2004). *Hierarchical Modeling and Analysis for Spatial Data*. Chapman and Hall/CRC Press, Boca Raton, FL.
- Beaumont, M. A., Zhang, W., and Balding, D. J. (2002). Approximate Bayesian computation in population genetics. *Genetics*, 162:2025–2035.
- Bevilacqua, M., Gaetan, C., Mateu, J., and Porcu, E. (2012). Estimating space and space-time covariance functions for large data sets: A weighted composite likelihood approach. *Journal of the American Statistical Association*, 107:268–280.
- Bezanson, J., Edelman, A., Karpinski, S., and Shah, V. B. (2017). Julia: A fresh approach to numerical computing. *SIAM Review*, 59:65–98.
- Casella, G. and Berger, R. (2001). *Statistical Inference*. Duxbury, Belmont, CA, second edition.
- Castruccio, S., Huser, R., and Genton, M. G. (2016). High-order composite likelihood inference for max-stable distributions and processes. *Journal of Computational and Graphical Statistics*, 25:1212–1229.
- Chan, J., Perrone, V., Spence, J., Jenkins, P., Mathieson, S., and Song, Y. (2018). A likelihood-free inference framework for population genetic data using exchangeable neural networks. In Bengio, S., Wallach, H., Larochelle, H., Grauman, K., Cesa-Bianchi, N., and Garnett, R., editors, *Advances in Neural Information Processing Systems*, volume 31. Curran Associates, Inc.
- Chen, Y., Zhang, D., Gutmann, M. U., Courville, A., and Zhu, Z. (2021). Neural approximate sufficient statistics for implicit models. In *Proceedings of the 9th International Conference on Learning Representations, ICLR*.
- Chon, K. and Cohen, R. (1997). Linear and nonlinear ARMA model parameter estimation using an artificial neural network. *IEEE Transactions on Biomedical Engineering*, 44:168–174.

- Cox, D. and Reid, N. (2004). A note on pseudolikelihood constructed from marginal densities. *Biometrika*, 3:729–737.
- Cressie, N. (1993). *Statistics for Spatial Data*. Wiley, Hoboken, NJ, revised edition.
- Cressie, N. and Wikle, C. K. (2011). *Statistics for Spatio-Temporal Data*. Wiley, Hoboken, NJ.
- Davison, A. C., Huser, R., and Thibaud, E. (2019). Spatial extremes. In Gelfand, A. E., Fuentes, M., Hoeting, J. A., and Smith, R. L., editors, *Handbook of Environmental and Ecological Statistics*, pages 711–744. Chapman & Hall/CRC Press, Boca Raton, FL.
- Diggle, P. J. and Gratton, R. J. (1984). Monte Carlo methods of inference for implicit statistical models. *Journal of the Royal Statistical Society B*, 46:193–227.
- Diggle, P. J. and Ribeiro, P. J. (2007). *Model-Based Geostatistics*. Springer, New York, NY.
- Donlon, C. J., Martin, M., Stark, J., Roberts-Jones, J., Fiedler, E., and Wimmer, W. (2012). The operational sea surface temperature and sea ice analysis (OSTIA) system. *Remote Sensing of Environment*, 116:140–158.
- Flagel, L., Brandvain, Y., and Schrider, D. R. (2018). The unreasonable effectiveness of convolutional neural networks in population genetic inference. *Molecular Biology and Evolution*, 36:220–238.
- Gaskin, T., Pavliotis, G. A., and Girolami, M. (2023). Neural parameter calibration for large-scale multiagent models. *Proceedings of the National Academy of Sciences*, 120(7):e2216415120.
- Gerber, F. and Nychka, D. W. (2021). Fast covariance parameter estimation of spatial Gaussian process models using neural networks. *Stat*, 10:e382.
- Goodfellow, I., Bengio, Y., and Courville, A. (2016). *Deep Learning*. MIT Press, Cambridge, MA.
- Han, J., Li, Y., Lin, L., Lu, J., Zhang, J., and Zhang, L. (2022). Universal approximation of symmetric and anti-symmetric functions. *Communications in Mathematical Sciences*, 20:1397–1408.
- Hazra, A. and Huser, R. (2021). Estimating high-resolution Red Sea surface temperature hotspots, using a low-rank semiparametric spatial model. *Annals of Applied Statistics*, 15:572–596.
- Heffernan, J. E. and Tawn, J. A. (2004). A conditional approach for multivariate extreme values. *Journal of the Royal Statistical Society B*, 66:497–546.
- Hornik, K., Stinchcombe, M., and White, H. (1989). Multilayer feedforward networks are universal approximators. *Neural Networks*, 2:359–366.
- Hrafnkelsson, B., Siegert, S., Huser, R., Bakka, H., and Johannesson, A. V. (2021). Max-and-Smooth: a two-step approach for approximate Bayesian inference in latent Gaussian models. *Bayesian Analysis*, 16:611–638.
- Huser, R. (2021). Editorial: EVA 2019 data competition on spatio-temporal prediction of Red Sea surface temperature extremes. *Extremes*, 24:91–104.
- Huser, R. and Davison, A. C. (2013). Composite likelihood estimation for the Brown–Resnick process. *Biometrika*, 100:511–518.
- Huser, R., Dombry, C., Ribatet, M., and Genton, M. G. (2019). Full likelihood inference for max-stable data. *Stat*, 8:e218.
- Huser, R., Stein, M. L., and Zhong, P. (2022). Vecchia likelihood approximation for accurate and fast inference in intractable spatial extremes models. *arXiv:2203.05626v1*.
- Huser, R. and Wadsworth, J. (2022). Advances in statistical modeling of spatial extremes. *Wiley Interdisciplinary Reviews: Computational Statistics*, 14:e1537.
- Innes, M. (2018). Flux: Elegant machine learning with Julia. *Journal of Open Source Software*, 3:602.
- Jiang, B., Wu, T.-Y., Zheng, C., and Wong, W. H. (2017). Learning summary statistic for approximate Bayesian computation via deep neural network. *Statistica Sinica*, 27:1595–1618.

- Lehmann, E. L. and Casella, G. (1998). *Theory of Point Estimation*. Springer, New York, NY, 2nd edition.
- Lenzi, A., Bessac, J., Rudi, J., and Stein, M. L. (2021). Neural networks for parameter estimation in intractable models. *arXiv:2107.14346v1*.
- Lintusaari, J., Gutmann, M., Dutta, R., Kaski, S., and Corander, J. (2017). Fundamentals and recent developments in approximate Bayesian computation. *Systematic Biology*, 66:66–82.
- McCullagh, P. (2002). What is a statistical model. *The Annals of Statistics*, 30:1225–1310.
- Murphy, R. L., Srinivasan, B., Rao, V. A., and Ribeiro, B. (2019). Janossy pooling: Learning deep permutation-invariant functions for variable-size inputs. In *7th International Conference on Learning Representations, ICLR*.
- Nelder, J. A. and Mead, R. (1965). A simplex method for function minimization. *The Computer Journal*, 7:308–313.
- Pacchiardi, L. and Dutta, R. (2022). Likelihood-free inference with generative neural networks via scoring rule minimization. *arXiv:2205.15784*.
- Padoan, S. A., Ribatet, M., and Sisson, S. A. (2010). Likelihood-based inference for max-stable processes. *Journal of the American Statistical Association*, 105:263–277.
- Papamakarios, G., Nalisnick, E., Rezende, D. J., and Lakshminarayanan, S. M. B. (2021). Normalizing flows for probabilistic modeling and inference. *Journal of Machine Learning Research*, 22:1–64.
- Radev, S. T., Mertens, U. K., Voss, A., Ardizzone, L., and Köthe, U. (2022). BayesFlow: Learning complex stochastic models with invertible neural networks. *IEEE Transactions on Neural Networks and Learning Systems*, 33:1452–1466.
- Ramesh, P., Lueckmann, J.-M., Boelts, J., Tejero-Cantero, A., Greenberg, D., Goncalves, P., and Macke, J. (2022). GATSBI: Generative adversarial training for simulation-based inference. In *Proceedings of the 10th International Conference on Learning Representations, ICLR*.
- Raynal, L., Marin, J.-M., Pudlo, P., Ribatet, M., Robert, C. P., and Estoup, A. (2018). ABC random forests for Bayesian parameter inference. *Bioinformatics*, 35:1720–1728.
- R Core Team (2023). *R: A Language and Environment for Statistical Computing*. R Foundation for Statistical Computing, Vienna, Austria.
- Richards, J., Tawn, J. A., and Brown, S. (2021). Modelling extremes of spatial aggregates of precipitation using conditional methods. *Annals of Applied Statistics*, in press.
- Rudi, J., Julie, B., and Lenzi, A. (2021). Parameter estimation with dense and convolutional neural networks applied to the FitzHugh-Nagumo ODE. In Bruna, J., Hesthaven, J., and Zdeborova, L., editors, *Proceedings of the 2nd Annual Conference on Mathematical and Scientific Machine Learning*, volume 145 of *Proceedings of Machine Learning Research*, pages 1–28. PMLR.
- Rue, H., Martino, S., and Chopin, N. (2009). Approximate Bayesian inference for latent Gaussian models by using integrated nested Laplace approximations. *Journal of the Royal Statistical Society B*, 71:319–392.
- Sang, H. and Genton, M. G. (2012). Tapered composite likelihood for spatial max-stable models. *Spatial Statistics*, 8:86–103.
- Schlather, M. (2002). Models for stationary max-stable random fields. *Extremes*, 5:33–44.
- Simpson, E. S., Opitz, T., and Wadsworth, J. L. (2021). High-dimensional modeling of spatial and spatio-temporal conditional extremes using INLA and the SPDE approach. *arXiv:2011.04486v2*.
- Simpson, E. S. and Wadsworth, J. L. (2021). Conditional modelling of spatio-temporal extremes for Red Sea surface temperatures. *Spatial Statistics*, 41:100482.

- Sisson, S. A. and Fan, Y. (2011). Likelihood-free MCMC. In Brooks, S., Gelman, A., Jones, G., and Meng, X.-L., editors, *Handbook of Markov Chain Monte Carlo*, pages 313–335. Chapman & Hall/CRC Press, Boca Raton, FL.
- Sisson, S. A., Fan, Y., and Beaumont, M. (2018). *Handbook of Approximate Bayesian Computation*. Chapman & Hall/CRC Press, Boca Raton, FL.
- Sisson, S. A., Fan, Y., and Tanaka, M. (2007). Sequential Monte Carlo without likelihoods. *Proceedings of the National Academy of Sciences*, 104:1760–1765.
- Soelch, M., Akhundov, A., van der Smagt, P., and Bayer, J. (2019). On Deep Set learning and the choice of aggregations. In Tetko, I. V., Kurková, V., Karpov, P., and Theis, F. J., editors, *Proceedings of the 28th International Conference on Artificial Neural Networks, ICANN*, Lecture Notes in Computer Science, pages 444–457. Springer.
- Stein, M. L. (1999). *Interpolation of Spatial Data: Some Theory for Kriging*. Springer, New York, NY.
- Stein, M. L., Chi, Z., and Welty, L. J. (2004). Approximating likelihoods for large spatial data sets. *Journal of the Royal Statistical Society B*, 66:275–296.
- Strasser, H. (1981). Consistency of maximum likelihood and Bayes estimates. *The Annals of Statistics*, 9:1107–1113.
- Subbotin, M. T. (1923). On the law of frequency of errors. *Mathematicheskii Sbornik*, 31:296–301.
- Varin, C., Reid, N., and Firth, D. (2011). An overview of composite likelihood methods. *Statistica Sinica*, 21:5–42.
- Varin, C. and Vidoni, P. (2005). A note on composite likelihood inference and model selection. *Biometrika*, 92:519–528.
- Vecchia, A. V. (1988). Estimation and model identification for continuous spatial processes. *Journal of the Royal Statistical Society B*, 50:297–312.
- Wadsworth, J. L. and Tawn, J. A. (2022). Higher-dimensional spatial extremes via single-site conditioning. *Spatial Statistics*, 51:100677.
- Wagstaff, E., Fuchs, F. B., Engelcke, M., Osborne, M., and Posner, I. (2022). Universal approximation of functions on sets. *Journal of Machine Learning Research*, 23:1–56.
- Wagstaff, E., Fuchs, F. B., Engelcke, M., Posner, I., and Osborne, M. (2019). On the limitations of representing functions on sets. In Chaudhuri, K. and Salakhutdinov, R., editors, *Proceedings of the 36th International Conference on Machine Learning*, volume 97, pages 6487–6494. PMLR.
- Wiqvist, S., Mattei, P.-A., Picchini, U., and Frellsen, J. (2019). Automatic posterior transformation for likelihood-free inference. In Chaudhuri, K. and Salakhutdinov, R., editors, *Proceedings of the 36th International Conference on Machine Learning*, volume 97 of *Proceedings of Machine Learning Research*, pages 6798–6807. PMLR.
- Wu, Z., Pan, S., Chen, F., Long, G., Zhang, C., and Yu, P. S. (2021). A comprehensive survey on graph neural networks. *IEEE Transactions on Neural Networks and Learning Systems*, 32:4–24.
- Zaheer, M., Kottur, S., Ravanbakhsh, S., Poczos, B., Salakhutdinov, R. R., and Smola, A. J. (2017). Deep sets. In Guyon, I., Luxburg, U. V., Bengio, S., Wallach, H., Fergus, R., Vishwanathan, S., and Garnett, R., editors, *Advances in Neural Information Processing Systems*, volume 30. Curran Associates, Inc.
- Zammit-Mangion, A. and Wikle, C. K. (2020). Deep integro-difference equation models for spatio-temporal forecasting. *Spatial Statistics*, 37:100408.
- Zhang, H. (2004). Inconsistent estimation and asymptotically equal interpolations in model-based geostatistics. *Journal of the American Statistical Association*, 99:250–261.
- Zhou, D. (2018). Universality of deep convolutional neural networks. *Applied and Computational Harmonic Analysis*, 48:787–794.

Supplementary Material for “Neural Point Estimation for Fast Optimal Likelihood-Free Inference”

This document contains supplementary material for the paper “Neural Point Estimation for Fast Optimal Likelihood-Free Inference”. In Sections [S1](#) and [S2](#), we conduct experiments to illustrate the benefits of pre-training and “on-the-fly” simulation, respectively. In Section [S3](#), we describe how we simulate from the models considered in Section 4 of the main text, and we provide the density functions required for the corresponding likelihood-based estimators. In Section [S4](#), we describe our analysis for a Gaussian process model that is simpler than that considered in the main text, namely, the Gaussian process model with known smoothness. In Section [S5](#), we detail the bootstrap techniques used in Section 5 of the main text. In Section [S6](#), we apply our methodology to the analysis of sea-surface temperature data in the Red Sea, where the data are measured irregularly in space. In Section [S7](#), we provide some empirical evidence that our neural Bayes estimators can extrapolate beyond the sample space of the assumed model reasonably well. Finally, in Section [S8](#), we provide additional exploratory and diagnostic plots for the experiments given in the main text.

S1 Motivation for pre-training

Recall that the parameters of a neural network trained for one task can provide useful initial values for the parameters of another neural network intended for a slightly different task. This is known as pre-training ([Goodfellow et al., 2016](#), Ch. 8). To illustrate the benefits of pre-training in the context of neural parameter estimation, Figure [S1](#) shows the validation risk (i.e., the risk evaluated using ϑ_{val} and \mathcal{Z}_{val}) during training for two neural estimators for the Gaussian process model of Section 4.2 of the main text. Both were trained with $m = 30$ independent replicates available for each parameter configuration, but only one was pre-trained with a neural estimator trained with $m = 1$ independent replicate. Although both estimators eventually converge to a similar risk, the pre-trained estimator converges in drastically fewer epochs.

S2 Motivation for “on-the-fly” simulation

Recall that the ease with which data can be simulated from the models that we are concerned with means that $\mathcal{Z}_{\text{train}}$ can often be simulated periodically during training, a technique that [Chan et al. \(2018\)](#) call “simulation-on-the-fly”. Here, we conduct an experiment to illustrate the benefits of this strategy. We train several neural estimators for the parameters of the Gaussian process model with known smoothness, as detailed in Section [S4](#). We consider three simulation-on-the-fly training routines; refreshing $\mathcal{Z}_{\text{train}}$ every epoch, refreshing $\mathcal{Z}_{\text{train}}$ every 30 epochs, and keeping $\mathcal{Z}_{\text{train}}$ fixed. We also consider two neural network architectures that differ only in the width of each layer; the first contains roughly 600,000 trainable parameters, while the second contains an order-of-magnitude fewer. All other components in the experiment (e.g., the size of $\mathcal{Z}_{\text{train}}$, here equal to 100,000) are held fixed.

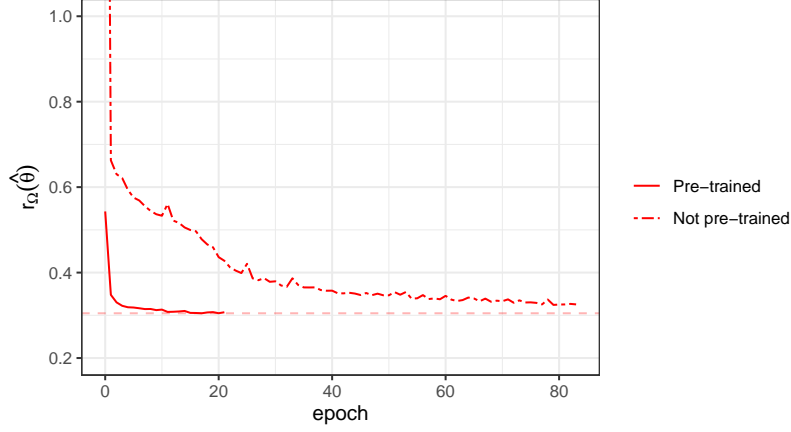


Figure S1: The risk function with respect to the absolute error loss evaluated on the validation set for two neural estimators, each trained with $m = 30$ independent replicates available for each parameter configuration. One estimator (solid line) was pre-trained with a neural estimator trained with $m = 1$ independent replicates, while the other (dashed-dotted line) was randomly initialised. The horizontal dashed line shows the minimum risk achieved by the pre-trained estimator.

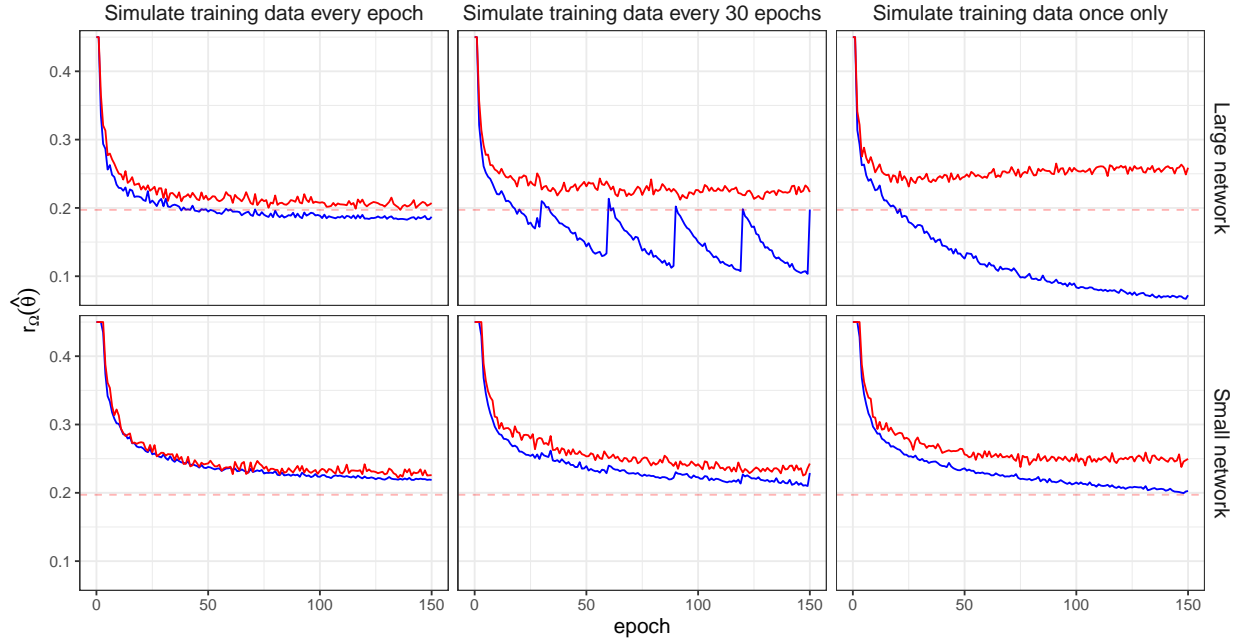


Figure S2: The risk with respect to the absolute error loss approximated using the training (blue) and validation (red) data sets for two neural network architectures (rows) and for three simulation-on-the-fly training routines (columns). The horizontal red dashed line shows the minimum validation risk achieved in the study, and all axes are fixed to facilitate comparison.

Figure S2 shows the risk evaluated during training for each combination of simulation-on-the-fly training routine and network architecture. Comparing the columns of the figure reveals that regularly refreshing $\mathcal{Z}_{\text{train}}$ clearly reduces overfitting, as measured by the discrepancy between training and validation risk. Due to this property, one may use larger,

more-representationally-powerful neural networks that are prone to overfitting when $\mathcal{Z}_{\text{train}}$ is fixed, and this leads to lower out-of-sample error, as seen when comparing the two panels in the first column of Figure S2.

Compared with fixing $\mathcal{Z}_{\text{train}}$, on-the-fly simulation can be computationally expensive. However, one may mimic on-the-fly simulation to avoid excessive computational cost. Specifically, to train a neural estimator for sample size m , one may simulate $\mathcal{Z}_{\text{train}}$ with each element containing m^* replicates, where m^* is a multiple of m ; then, during training, one may continuously cycle through the replicates of $\mathcal{Z}_{\text{train}}$ using m replicates per epoch. This approach mimics on-the-fly simulation in the sense that consecutive epochs use different training data, and it is particularly useful when training a piecewise neural estimator (recall Equation (8) of the main text).

S3 Model simulation and density functions

We now describe how we simulate from the models considered in Section 4 of the main text, and we provide the density functions required for the corresponding likelihood-based estimators.

S3.1 Gaussian process model

Recall our formulation of the Gaussian process model from Section 4.2 of the main text. We consider a classical spatial model, the linear Gaussian-Gaussian model,

$$Z_{ij} = Y_i(\mathbf{s}_j) + \epsilon_{ij}, \quad i = 1, \dots, m, \quad j = 1, \dots, n, \quad (11 \text{ revisited})$$

where $\mathbf{Z}_i \equiv (Z_{i1}, \dots, Z_{in})'$ are data observed at locations $\{\mathbf{s}_1, \dots, \mathbf{s}_n\}$ on a spatial domain \mathcal{D} , $\{Y_i(\cdot)\}$ are i.i.d. spatially-correlated mean-zero Gaussian processes, and $\epsilon_{ij} \sim N(0, \sigma_\epsilon^2)$ is Gaussian white noise. An important component of the model is the covariance function, $C(\mathbf{s}, \mathbf{u}) \equiv \text{cov}(Y_i(\mathbf{s}), Y_i(\mathbf{u}))$, for $\mathbf{s}, \mathbf{u} \in \mathcal{D}$ and $i = 1, \dots, m$. Here, we use the popular isotropic Matérn covariance function which, for $\mathbf{h} \equiv \mathbf{s} - \mathbf{u}$, is

$$C(\mathbf{s}, \mathbf{u}) = \sigma^2 \frac{2^{1-\nu}}{\Gamma(\nu)} \left(\frac{\|\mathbf{h}\|}{\rho} \right) K_\nu \left(\frac{\|\mathbf{h}\|}{\rho} \right), \quad (12 \text{ revisited})$$

with σ^2 the marginal variance, $\Gamma(\cdot)$ the gamma function, $K_\nu(\cdot)$ the Bessel function of the second kind of order ν , and $\rho > 0$ and $\nu > 0$ the range and smoothness parameters, respectively. Following Gerber and Nychka (2021), we fix $\sigma^2 = 1$. This leaves three (possibly) unknown parameters that need to be estimated: $\boldsymbol{\theta} \equiv (\sigma_\epsilon, \rho, \nu)'$.

Let \mathbf{L} denote the lower Cholesky factor of the covariance matrix

$$\mathbf{C} \equiv (C(\mathbf{s}_j, \mathbf{s}_{j'}) : j, j' = 1, \dots, n).$$

Then, simulation from (11) proceeds with Algorithm S1 and, for a single replicate, the

Algorithm S1 Simulation from the mean-zero Gaussian process model

Require: Parameters ρ , ν , and σ_ϵ ; sample size m .

- 1: Compute \mathbf{C} , the covariance matrix with entries $C(\mathbf{s}_j, \mathbf{s}_{j'})$ for $j, j' = 1, \dots, n$.
 - 2: Compute \mathbf{L} , the lower Cholesky factor of \mathbf{C} .
 - 3: **for** $i = 1, \dots, m$ **do**
 - 4: Simulate $\mathbf{w}_i \sim \mathcal{N}(\mathbf{0}, \mathbf{I})$.
 - 5: Simulate $\boldsymbol{\epsilon}_i \sim \mathcal{N}(\mathbf{0}, \sigma_\epsilon^2 \mathbf{I})$.
 - 6: Set $\mathbf{Y}_i = \mathbf{L}\mathbf{w}_i$.
 - 7: Set $\mathbf{Z}_i = \mathbf{Y}_i + \boldsymbol{\epsilon}_i$.
 - 8: **end for**
 - 9: Return $\mathbf{Z} \equiv (\mathbf{Z}'_1, \dots, \mathbf{Z}'_m)'$.
-

log-likelihood function for (11) is

$$\begin{aligned} \ell(\boldsymbol{\theta}; \mathbf{Z}_i) &= -\frac{n}{2} \log 2\pi - \frac{1}{2} \log |\boldsymbol{\Sigma}_i| - \frac{1}{2} \mathbf{Z}'_i \boldsymbol{\Sigma}_i^{-1} \mathbf{Z}_i \\ &= -\frac{n}{2} \log 2\pi - \sum_{j=1}^n \log L_{jj} - \frac{1}{2} \mathbf{u}'_i \mathbf{u}_i, \end{aligned}$$

where $\boldsymbol{\Sigma} \equiv \text{cov}(\mathbf{Z}_i, \mathbf{Z}_i) = \mathbf{C} + \sigma_\epsilon^2 \mathbf{I}$ with \mathbf{I} the identity matrix, L_{jj} is the j th diagonal element of \mathbf{L} , and \mathbf{u}_i is the solution to $\mathbf{L}\mathbf{u}_i = \mathbf{Z}_i$ which, since \mathbf{L} is lower-triangular, can be computed using an efficient forward solve.

S3.2 Schlather's max-stable model

Recall Schlather's max-stable model from Section 4.3 of the main text, given by

$$Z_{ij} = \bigvee_{k \in \mathbb{N}} \zeta_{ik} \max\{0, Y_{ik}(\mathbf{s}_j)\}, \quad i = 1, \dots, m, \quad j = 1, \dots, n, \quad (13 \text{ revisited})$$

where \bigvee denotes the maximum over the indexed terms, $\mathbf{Z}_i \equiv (Z_{i1}, \dots, Z_{in})'$ are data observed at locations $\{\mathbf{s}_1, \dots, \mathbf{s}_n\} \subset \mathcal{D}$, $\{\zeta_{ik} : k \in \mathbb{N}\}$ for $i = 1, \dots, m$ are i.i.d. Poisson point processes on $(0, \infty)$ with intensity measure $d\Lambda(\zeta) = \zeta^{-2} d\zeta$, and $\{Y_{ik}(\cdot) : i = 1, \dots, m, k \in \mathbb{N}\}$ are i.i.d. mean-zero Gaussian processes scaled so that $\mathbb{E}[\max\{0, Y_{ik}(\cdot)\}] = 1$. We model each $Y_{ik}(\cdot)$ using the Matérn covariance function, (12), with $\sigma^2 = 1$. Hence, $\boldsymbol{\theta} \equiv (\rho, \nu)'$.

We use Algorithm S2 for approximate simulation from (13), which was given by Schlather (2002) (see also Dey and Yan, 2016, alg. 1.2.2). The tuning parameter R involves a trade-off between computational efficiency (favouring small R) and accuracy (favouring large R). Schlather (2002) recommends the use of $R = 3$; conservatively, we set $R = 3.5$.

Recall that we compare our neural estimator to the pairwise maximum a posteriori (MAP) estimator, which is simply the MAP estimator with the log-likelihood function replaced with the pairwise log-likelihood function. Further recall that, in general, the pairwise log-likelihood function for the i th replicate is

$$\ell_P(\boldsymbol{\theta}; \mathbf{Z}_i) \equiv \sum_{j=1}^{n-1} \sum_{j'=j+1}^n \log f(Z_{ij}, Z_{ij'}; \boldsymbol{\theta}), \quad (14 \text{ revisited})$$

Algorithm S2 Simulation from Schlather's max-stable model

Require: Positive R ; parameters ρ and ν ; sample size m .

- 1: Compute \mathbf{C} , the covariance matrix with entries $C(\mathbf{s}_j, \mathbf{s}_{j'})$ for $j, j' = 1, \dots, n$.
 - 2: Compute \mathbf{L} , the lower Cholesky factor of \mathbf{C} .
 - 3: **for** $i = 1, \dots, m$ **do**
 - 4: Set $\mathbf{Z}_i = \mathbf{0}$.
 - 5: Simulate $\zeta_i^{-1} \sim \text{Exp}(1)$.
 - 6: **while** $R\zeta_i > \min\{\mathbf{Z}_i\}$ **do**
 - 7: Denote the current iteration by k .
 - 8: Set $\mathbf{Y}_{ik} = \mathbf{L}\mathbf{w}_k$ where $\mathbf{w}_k \sim N(\mathbf{0}, \mathbf{I})$.
 - 9: Set $Z_{ij} = \max(Z_{ij}, \zeta_i Y_{ikj})$ for $j = 1, \dots, n$.
 - 10: Update ζ_i^{-1} by $\zeta_i^{-1} + E_k$, where $E_k \sim \text{Exp}(1)$.
 - 11: **end while**
 - 12: Set $\mathbf{Z}_i = (Z_{i1}, \dots, Z_{in})'$.
 - 13: **end for**
 - 14: Return $\mathbf{Z} \equiv (\mathbf{Z}'_1, \dots, \mathbf{Z}'_m)'$.
-

where $f(\cdot, \cdot; \boldsymbol{\theta})$ denotes the bivariate probability density function for pairs in \mathbf{Z}_i . The bivariate cumulative distribution function for max-stable models with unit Fréchet margins (e.g., Schlather's model) is of the form (Huser, 2013, pg. 231–232),

$$F(z_1, z_2; \boldsymbol{\theta}) = \exp\{-V(z_1, z_2)\},$$

where $V(\cdot, \cdot)$ is the so-called exponent function. Then, by the chain rule,

$$f(z_1, z_2; \boldsymbol{\theta}) = \frac{\partial}{\partial z_1 \partial z_2} F(z_1, z_2) = \{V_1(z_1, z_2)V_2(z_1, z_2) - V_{12}(z_1, z_2)\} \exp\{-V(z_1, z_2)\},$$

where V_1 , V_2 , and V_{12} denote the partial derivatives of V with respect to z_1 , z_2 , and both z_1 and z_2 , respectively. Now, for $(Z_1, Z_2)'$ drawn from Schlather's max-stable model (13) and observed at locations $\mathbf{s}_1, \mathbf{s}_2 \in \mathcal{D}$, respectively, we have

$$\begin{aligned} V(z_1, z_2) &= \left(\frac{1}{z_1} + \frac{1}{z_2}\right) \left[1 - \frac{1}{2} \left(1 - \frac{1}{z_1 + z_2} \{z_1^2 - 2z_1 z_2 \psi + z_2^2\}^{1/2}\right)\right], \\ V_1(z_1, z_2) &= -\frac{1}{2z_1^2} + \frac{1}{2} \left(\frac{\psi}{z_1} - \frac{z_2}{z_1^2}\right) (z_1^2 - 2z_1 z_2 \psi + z_2^2)^{-1/2}, \\ V_2(z_1, z_2) &= V_1(z_2, z_1), \\ V_{12}(z_1, z_2) &= -\frac{1}{2} (1 - \psi^2) (z_1^2 - 2z_1 z_2 \psi + z_2^2)^{-3/2}, \end{aligned}$$

where $\psi \equiv \text{corr}(Y(\mathbf{s}_1), Y(\mathbf{s}_2))$ depends on $\boldsymbol{\theta}$.

S3.3 Spatial conditional extremes model

Recall our formulation of the spatial conditional extremes model from Section 4.4, which describes the behaviour of a process conditional on it being greater than some threshold, u ,

at a conditioning site, $\mathbf{s}_0 \in \mathcal{D}$. Specifically,

$$Z_{ij} \mid Z_{i0} > u \stackrel{d}{=} a(\mathbf{h}_j, Z_{i0}) + b(\mathbf{h}_j, Z_{i0})Y_i(\mathbf{s}_j), \quad i = 1, \dots, m, \quad j = 1, \dots, n \quad (15 \text{ revisited})$$

where ‘ $\stackrel{d}{=}$ ’ denotes equality in distribution, $Z_{i0} \equiv Z_i(\mathbf{s}_0)$ is the value of the data process at the conditioning site, $\mathbf{h}_j \equiv \mathbf{s}_j - \mathbf{s}_0$, and $Z_{i0} - u \mid Z_{i0} > u$ is a unit exponential random variable that is independent of the residual process, $Y_i(\cdot)$. We model $a(\cdot, \cdot)$ and $b(\cdot, \cdot)$ using parametric forms proposed by [Wadsworth and Tawn \(2022\)](#),

$$\begin{aligned} a(\mathbf{h}, z) &= z \exp\{-(\|\mathbf{h}\|/\lambda)^\kappa\}, \quad \lambda > 0, \quad \kappa > 0, \\ b(\mathbf{h}, z) &= 1 + a(\mathbf{h}, z)^\beta, \quad \beta > 0, \end{aligned}$$

where $\mathbf{h} \equiv \mathbf{s} - \mathbf{s}_0$ for $\mathbf{s} \in \mathcal{D}$ and $z \in \mathbb{R}$. We construct the residual process, $Y_i(\cdot)$, by first constructing the process $\tilde{Y}_i^{(0)}(\cdot) \equiv \tilde{Y}_i(\cdot) - \tilde{Y}_i(\mathbf{s}_0)$, where $\tilde{Y}_i(\cdot)$ is a mean-zero Gaussian process with Matérn covariance function and with unit marginal variance, and then marginally transforming it to the scale of a Subbotin distribution. We model δ as decaying from 2 to 1 as the distance to \mathbf{s}_0 increases; specifically,

$$\delta(\mathbf{h}) = 1 + \exp\{-(\|\mathbf{h}\|/\delta_1)^2\}, \quad \delta_1 > 0. \quad (16 \text{ revisited})$$

To describe simulation from (15), it is necessary to make several definitions. First, let $\tilde{C}(\cdot, \cdot)$ denote the covariance function of the i.i.d. processes $\{\tilde{Y}_i(\cdot) : i = 1, \dots, m\}$. Second, define $\tilde{Y}_i^{(01)}(\cdot) \equiv \tilde{Y}_i^{(0)}(\cdot)/\tilde{\sigma}^{(0)}(\cdot)$, where $\tilde{\sigma}^{(0)}(\cdot)$ is the standard-deviation process of $\tilde{Y}_i^{(0)}(\cdot)$. Finally, since $\tilde{Y}_i^{(01)}(\cdot)$ is a mean-zero Gaussian process with unit marginal variance, we obtain the Subbotin-scale residual process as $Y_i(\cdot) \equiv t(\tilde{Y}_i^{(01)}(\cdot))$, where $t(\cdot) \equiv Q_S(\Phi(\cdot))$, $\Phi(\cdot)$ is the distribution function of the standard univariate Gaussian distribution, and $Q_S(\cdot)$ is the quantile function of the delta-Laplace distribution (see below). Then, simulation from (15) proceeds with Algorithm S3.

S3.3.1 The delta-Laplace distribution

A delta-Laplace (generalised Gaussian) ([Subbotin, 1923](#)) distribution is parameterised by a location parameter $\mu \in \mathbb{R}$, a scale parameter $\tau > 0$, and a shape parameter $\delta > 0$. For $y \in \mathbb{R}$ and $p \in [0, 1]$, its density, distribution, and quantile functions are

$$\begin{aligned} f_S(y; \mu, \tau, \delta) &= \frac{\delta}{2\tau\Gamma(1/\delta)} \exp\left(-\left|\frac{y-\mu}{\tau}\right|^\delta\right), \\ F_S(y; \mu, \tau, \delta) &= \frac{1}{2} + \text{sign}(y - \mu) \frac{1}{2\Gamma(1/\delta)} \gamma\left(1/\delta, \left|\frac{y-\mu}{\tau}\right|^\delta\right), \\ Q_S(p; \mu, \tau, \delta) &= \text{sign}(p - 0.5) Q_G\left(2|p - 0.5|; \frac{1}{\delta}, \frac{1}{(k\tau)^\delta}\right)^{1/\delta} + \mu, \end{aligned}$$

where $\gamma(\cdot)$ is the unnormalised incomplete lower gamma function and $Q_G(\cdot)$ is the quantile function of the Gamma distribution.

Algorithm S3 Simulation from the spatial conditional extremes model

Require: Parameters $\rho, \nu, \kappa, \lambda, \beta, \mu, \tau$, and δ_1 ; extremal threshold u ; sample size m .

- 1: Compute $\boldsymbol{\delta} = (\delta(\mathbf{h}_1), \dots, \delta(\mathbf{h}_n))'$.
 - 2: Compute $\tilde{\boldsymbol{\sigma}}^{(0)} = (\sigma^{(0)}(\mathbf{h}_1), \dots, \sigma^{(0)}(\mathbf{h}_n))'$.
 - 3: Compute $\tilde{\mathbf{C}} \equiv (\tilde{C}(\mathbf{s}_j, \mathbf{s}_{j'}) : j, j' = 1, \dots, n)$.
 - 4: Compute $\tilde{\mathbf{L}}$, the lower Cholesky factor of $\tilde{\mathbf{C}}$.
 - 5: **for** $i = 1, \dots, m$ **do**
 - 6: Simulate $Z_{i0} = u + E_i$, where $E_i \sim \text{Exp}(1)$.
 - 7: Simulate $\tilde{\mathbf{Y}}_i = \tilde{\mathbf{L}}\mathbf{w}_i$, where $\mathbf{w}_i \sim \text{N}(\mathbf{0}, \mathbf{I})$.
 - 8: Set $\tilde{\mathbf{Y}}_i^{(0)} = \tilde{\mathbf{Y}}_i - \tilde{\mathbf{Y}}_{i0}$, where subtraction is elementwise.
 - 9: Set $\tilde{\mathbf{Y}}_i^{(01)} = \tilde{\mathbf{Y}}_i^{(0)} / \tilde{\boldsymbol{\sigma}}^{(0)}$, where division is elementwise. Note that the element of $\tilde{\boldsymbol{\sigma}}^{(0)}$ associated with \mathbf{s}_0 is equal to zero; since $Z_{i0} \equiv Z_i(\mathbf{s}_0)$ is simulated independently, this is not a problem in practice.
 - 10: Set $\mathbf{Y}_i = t(\tilde{\mathbf{Y}}_i^{(01)})$ where $t(\cdot)$ is applied elementwise.
 - 11: Set $Z_{ij} = a(\mathbf{h}_j, Z_{i0}) + b(\mathbf{h}_j, Z_{i0})Y_{ij}$, for $j = 1, \dots, n$.
 - 12: Set $\mathbf{Z}_i = (Z_{i0}, Z_{i1}, \dots, Z_{in})'$.
 - 13: **end for**
 - 14: Return $\mathbf{Z} \equiv (\mathbf{Z}'_1, \dots, \mathbf{Z}'_m)'$.
-

S4 Gaussian process model with known smoothness

We now consider the Gaussian process model of Section 4.2 of the main text with the smoothness parameter, ν , fixed to 1. This leaves two estimable parameters, σ_ϵ and ρ , which are usually well-identified from just a single field. Note that this model was also considered by Gerber and Nychka (2021).

Recall that we denote the sets of parameters used for training, validating, and testing the neural estimator by ϑ_{train} , ϑ_{val} , and ϑ_{test} , respectively. Rather than randomly sampling from a prior measure $\Omega(\cdot)$, Gerber and Nychka (2021) used a stratified, deterministic design (we defer to Gerber and Nychka, 2021, for details). The use of a deterministic design still implies a prior measure but, unless the design is relatively simple (e.g., a regularly spaced grid), this prior is difficult to formulate analytically. Although one should sample from $\Omega(\cdot)$, to facilitate a comparison with the work of Gerber and Nychka (2021), here, we use the same ϑ_{train} and ϑ_{test} they used, which contain 40,200 and 900 parameter configurations, respectively. We choose ϑ_{val} to be similar to ϑ_{test} , with $|\vartheta_{\text{val}}| = 2,000$. These parameter sets are shown in Figure S3, with a small subset of parameters in ϑ_{test} chosen to represent a range of model behaviours highlighted in red.

In our experiments, we compare the neural estimators to a likelihood-based estimator, namely, the maximum a posteriori (MAP) estimator. The MAP estimator requires the prior measure, $\Omega(\cdot)$, to be known; since this is not known here, and because we found that prior information is needed to avoid unreasonable maximum likelihood estimates in certain cases, here we let $\sigma_\epsilon \sim \text{Unif}(0.001, 1.5)$ and $\rho \sim \text{Unif}(1, 30)$.

Figure S4 shows the risk, with respect to the squared error loss and the prior implied by the deterministic parameter-space design, against the number of independent replicates, m ,

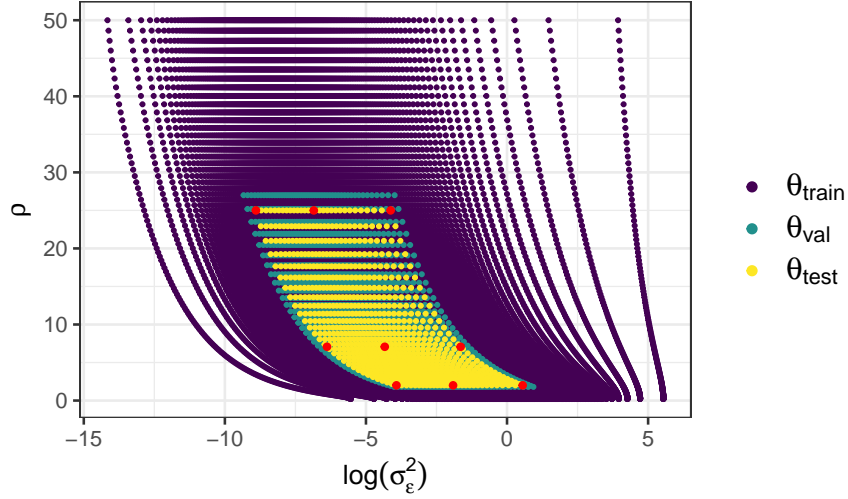


Figure S3: The sets of parameters ϑ_{train} , ϑ_{val} , and ϑ_{test} used in Section S4, shown in purple, green, and yellow, respectively. The small subset of parameters in ϑ_{test} chosen to represent a range of model behaviours is highlighted in red.

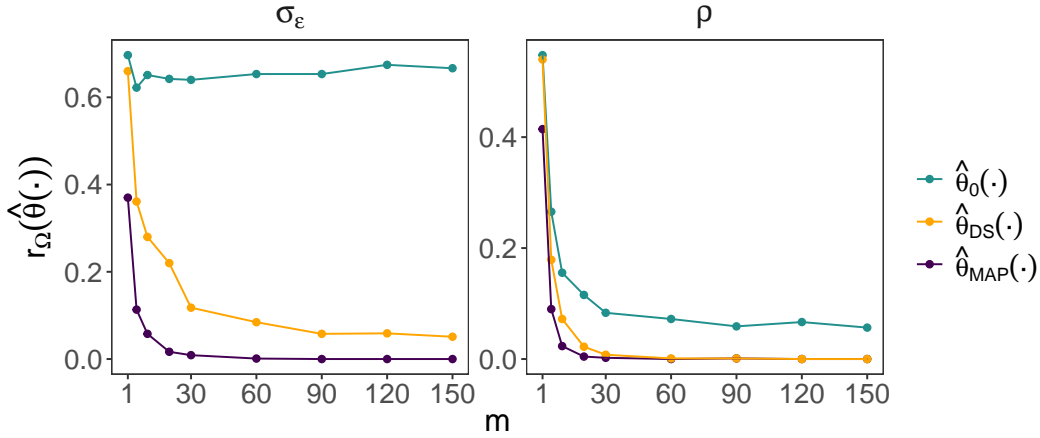


Figure S4: The risk with respect to the 0–1 loss against the number of replicates, m , available for each parameter vector in ϑ_{test} , for the estimators considered in Section S4. The estimators $\hat{\theta}_0(\cdot)$, $\hat{\theta}_{\text{DS}}(\cdot)$, and the MAP estimator are shown in green, orange, and purple, respectively.

available for the estimation of each parameter in ϑ_{test} . We also compare the empirical joint distributions of the estimators for several parameters in ϑ_{test} chosen to represent a range of model behaviours: Figure S5 shows the true parameters (red cross) and estimates obtained by applying each estimator to 100 sets of $m = 150$ independent model realisations. Overall, these results are in agreement with those given for the more complicated Gaussian process model considered in the main text, namely, that $\hat{\theta}_{\text{DS}}(\cdot)$ is a significant improvement over the prior art, $\hat{\theta}_0(\cdot)$, and it can incorporate information from an arbitrary number of replicates without a noticeable drop in estimation quality.

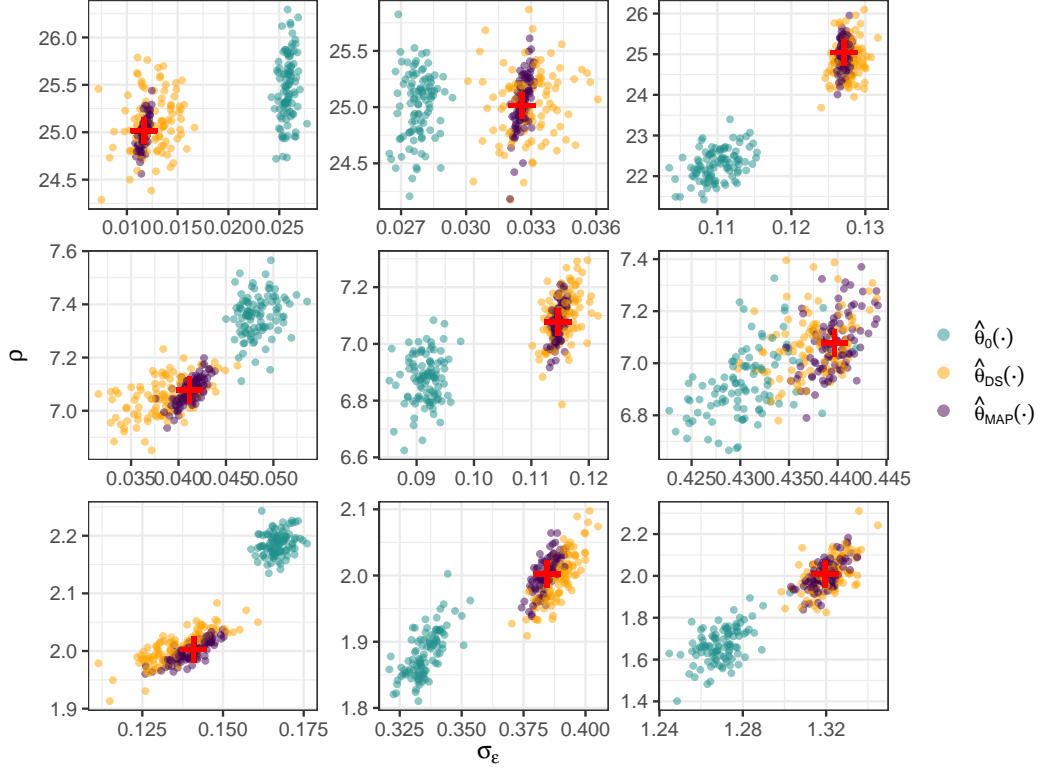


Figure S5: The empirical joint distribution of the estimators considered in Section S4, where each panel corresponds to one of the parameter vectors in ϑ_{test} (see Figure S3) intentionally chosen to capture a range of model behaviours (red). In accordance with Figure S3, the panels are ordered such that ρ increases moving from bottom to top, and σ_ϵ increases moving from left to right. The estimators $\hat{\theta}_0(\cdot)$, $\hat{\theta}_{DS}(\cdot)$, and the MAP estimator are shown in green, orange, and purple, respectively. Each estimate was obtained from a simulated data set of size $m = 150$.

S5 Bootstrapping in the Red Sea study

Here, we detail the bootstrap techniques used in Section 5 of the main text. Denote the observed data set as \mathbf{Z}^{obs} . To quantify the uncertainty in $\hat{\theta}(\mathbf{Z}^{\text{obs}})$ and the model-based estimates of the proportion of threshold exceedances in each region, we take the following approach.

- (i) Generate B pseudo replicates of \mathbf{Z}^{obs} (we set $B = 400$) and denote these replicates as $\mathbf{Z}_b^{\text{obs}}$, $b = 1, \dots, B$. To account for temporal dependence, evidence of which is displayed in Figure S15, we use a non-parametric-block bootstrap (Huser and Davison, 2014). Specifically, based on the assumption that fields between seasons are independent, we sample entire seasons with replacement.
- (ii) Using pseudo-replicate data, compute bootstrap estimates $\hat{\theta}(\mathbf{Z}_1^{\text{obs}}), \dots, \hat{\theta}(\mathbf{Z}_B^{\text{obs}})$; the 2.5 and 97.5 percentiles yield 95% bootstrap confidence intervals for θ .
- (iii) For each bootstrap estimate, simulate some large number, say, 1000 fields from $P_{\hat{\theta}(\mathbf{Z}_b^{\text{obs}})}$, generating B simulated data sets each with 1000 field replicates.

- (iv) Using these simulated data sets, compute B estimates of the proportion of threshold exceedances in each region, from which bootstrap confidence intervals are obtained through the appropriate quantiles.

Note that the finite sample size of \mathbf{Z}^{obs} makes the empirical estimates of the proportion of threshold exceedances in each region susceptible to noise; the pseudo replicates of \mathbf{Z}^{obs} also account for this uncertainty, since they are each approximately of the same size as \mathbf{Z}^{obs} (approximately because the blocks vary in size).

S6 Red Sea data: Irregularly-spaced locations

We now consider a second data set in the Red Sea, obtained by randomly selecting 678 irregularly-spaced locations from the full data set. To cater for irregular spatial data, which cannot be processed with CNNs directly, [Gerber and Nychka \(2021\)](#) suggest first computing the empirical variogram from the spatial data, and using this variogram as the input to a CNN. The variogram, however, is based on the second moment of the data only, and it is unlikely to contain sufficient information for inference with complex models, such as the spatial conditional extremes model. Instead, we construct our neural estimator using dense neural networks (DNNs). Specifically, we use a piecewise neural estimator in the same form as $\hat{\theta}_{\text{DS}}(\cdot)$ of the main text, with $\psi(\cdot)$ and $\phi(\cdot)$ constructed using the first two and last two rows of Table S1, respectively.

DNN-based estimators ignore the dependence structure present in spatial data, treating each datum as an independent input, and this typically results in a loss of statistical efficiency (see, e.g., [Rudi et al., 2021](#)). It is difficult to directly compare the CNN-based estimator of Section 5 of the main text with a DNN-based estimator for the present data, since these estimators are trained and assessed on different data sets. Hence, for the purpose of comparison, we also train a DNN-based estimator using the regular Red Sea data set considered in Section 5 of the main text. We denote the CNN-based and DNN-based estimators trained on the regular data set by $\hat{\theta}_{\text{CNN:reg}}(\cdot)$ and $\hat{\theta}_{\text{DNN:reg}}(\cdot)$, respectively, and we denote the DNN-based estimator trained for the irregular data set by $\hat{\theta}_{\text{DNN}}(\cdot)$. Figure S6 shows the risk with respect to the absolute-error loss against the number of independent replicates, m , available for the estimation of each parameter in ϑ_{test} . The DNN-based estimators perform similarly irrespective of whether the data are regular or irregular and, in agreement with [Rudi et al. \(2021\)](#), they are less efficient than the CNN-based estimator.

Table S2 gives estimates from the irregularly-spaced Red Sea data set which are similar to those obtained from the regularly-spaced data set. One disagreement lies in the estimates for ν and ρ , but these parameters are negatively correlated and, hence, the two sets of estimates are likely to lead to similar models, as reflected by the diagnostic plots given in Figures S7 and S8. Overall, the DNN-based estimator seems to be adequate for inference from these irregular spatial data. However, it is clearly sub-optimal, and future work will investigate the use of graphical neural networks (GNNs; see, e.g., [Wu et al., 2021](#)), which generalise the convolution operation to irregular spatial data.

Table S1: Summary of the neural network architecture used Section S6. We follow the convention of reporting the dimension of the input array and output array of each layer. Here, the dimension of the input array to the first layer, 678, is the number of spatial locations, n , in the data set considered in Section S6, and the dimension of the array output from the final layer is the number of parameters, p , in the spatial conditional extremes model.

layer type	activation function	input shape	output shape	weights
dense	ReLU	[678]	[300]	203,700
dense	ReLU	[300]	[100]	30,100
dense	ReLU	[100]	[50]	5,050
dense	identity	[50]	[8]	408
total trainable parameters:				239,258

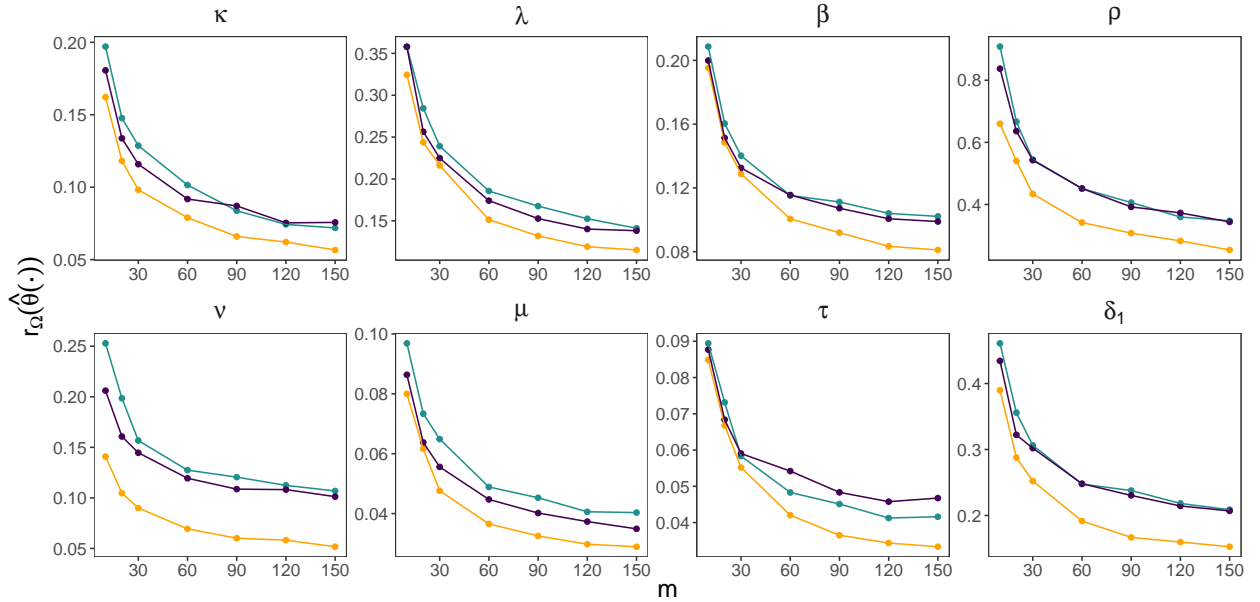


Figure S6: The risk with respect to the absolute-error loss against the number of replicates, m , available for each parameter vector in ϑ_{test} , for the estimators considered in Section S6. The estimators $\hat{\theta}_{\text{DNN}}(\cdot)$, $\hat{\theta}_{\text{DNN:reg}}(\cdot)$, and $\hat{\theta}_{\text{CNN:reg}}(\cdot)$ are shown in green, purple, and orange, respectively.

Table S2: Parameter estimates and 95% bootstrap confidence intervals (provided via the 2.5 and 97.5 percentiles of the bootstrap distribution) for the Red Sea data set considered in Section S6.

	κ	λ	β	ρ	ν	μ	τ	δ_1
Estimate	1.04	3.29	0.29	2.76	0.55	-0.02	0.63	2.03
2.5%	0.95	2.38	0.19	2.11	0.49	-0.10	0.53	1.40
97.5%	1.19	4.17	0.52	3.61	0.63	0.06	0.75	2.67

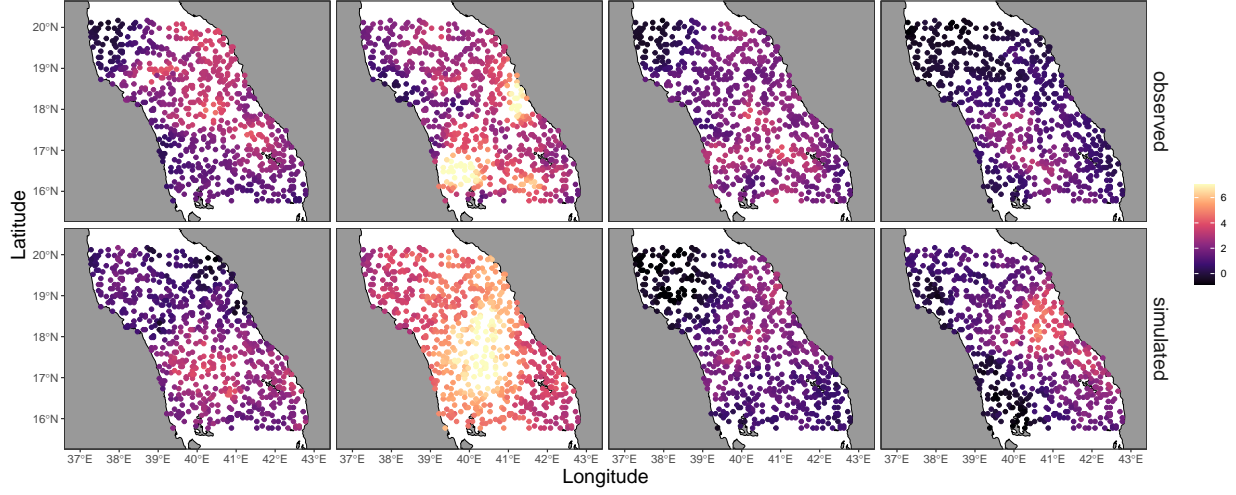


Figure S7: (Top row) Randomly-selected fields from the Red Sea data set considered in Section S6, where $Z(s_0) > u$. (Bottom row) Simulations from the fitted model. The data are overlaid on a map where the grey areas correspond to land (Sudan and Eritrea to the West, Saudi Arabia to the East) and the white areas correspond to sea.

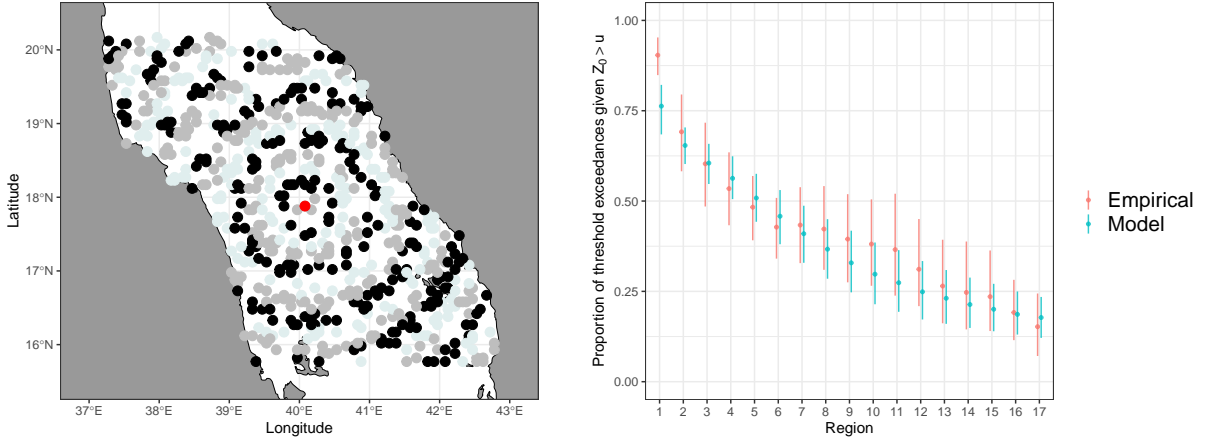


Figure S8: (Left) The spatial domain of interest for the Red Sea study of Section S6, with the conditioning site, s_0 , shown in red, and the remaining locations separated into 17 regions; the region labels begin at 1 in the centre of the domain and increase with distance from the centre. (Right) The estimated proportion of locations for which the process exceeds u given that it is exceeded at s_0 (points) and corresponding 95% confidence intervals (vertical segments) using model-simulated and empirical bootstrap data sets.

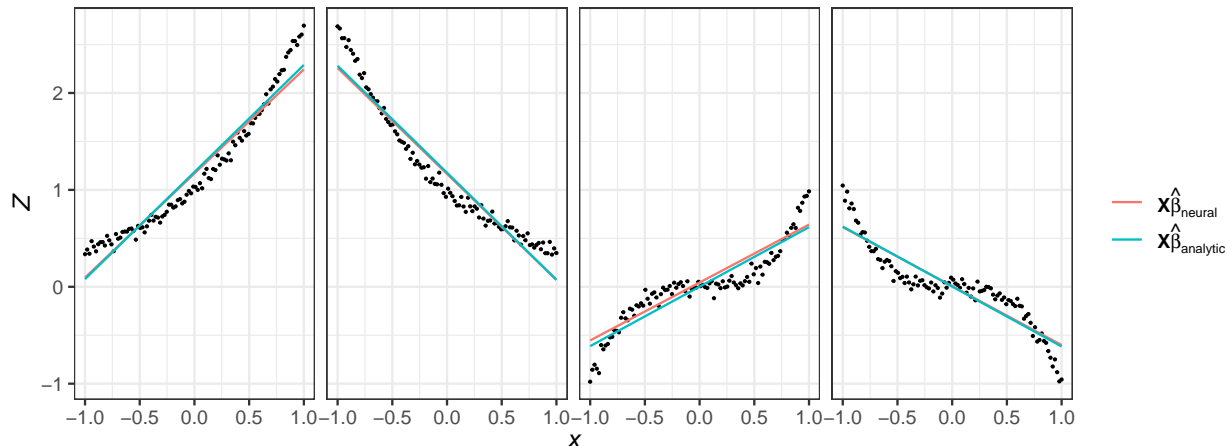


Figure S9: Fitted lines using the neural Bayes estimator (red) and the posterior median computed analytically (blue) given data simulated from several non-linear models (black points).

S7 Robustness to model misspecification

When the model is misspecified, the maximum likelihood (ML) estimator, under mild regularity conditions, asymptotically follows a Normal distribution centred on the value of θ that minimises the Kullback-Leibler divergence between the assumed model and the true model (Davison, 2003, pg. 147). Due to their asymptotic relation to the ML estimator, we can therefore expect that a large class of Bayes estimators exhibit similar behaviour under misspecification in the large sample case. During training, however, neural Bayes estimators are only exposed to simulations from the assumed model and, hence, there is a question as to whether they are suitable when the true model from which the observed data are generated is different from the model that they are trained on. Here, we provide some empirical evidence that neural estimators can extrapolate beyond the sample space of the assumed model.

We trained a neural Bayes estimator under a linear model, and applied it to several non-linear data sets. The assumed model is,

$$\mathbf{Z} = \mathbf{X}\boldsymbol{\beta} + \boldsymbol{\epsilon},$$

where $\mathbf{Z} \equiv (Z_1, \dots, Z_n)'$ is the data vector, $\boldsymbol{\beta} \equiv (\beta_0, \beta_1)'$ is a vector of regression parameters, \mathbf{X} is a design matrix containing a column of ones and a univariate covariate taking values between $[-1, 1]$, and $\boldsymbol{\epsilon} \sim N(\mathbf{0}, \sigma^2 \mathbf{I})$. Here, we set $n = 100$ and $\sigma = 0.05$. We used a conjugate Gaussian prior, $\boldsymbol{\beta} \sim N(\mathbf{0}, \mathbf{I})$.

Figure S9 shows the fitted lines using estimates from the neural Bayes estimator (red) and the posterior median of $\boldsymbol{\beta}$ computed analytically (blue) given data simulated from several non-linear models (black points). In each case, the neural Bayes estimator provides a similar fit to that based on the analytic posterior median. Hence, at least in this simple setting, neural Bayes estimators appear to have some extrapolative power beyond the sample space of the assumed model. The good results we obtained in the real experimental study add further evidence that neural Bayes estimators are robust to deviations from the true model.

S8 Additional figures

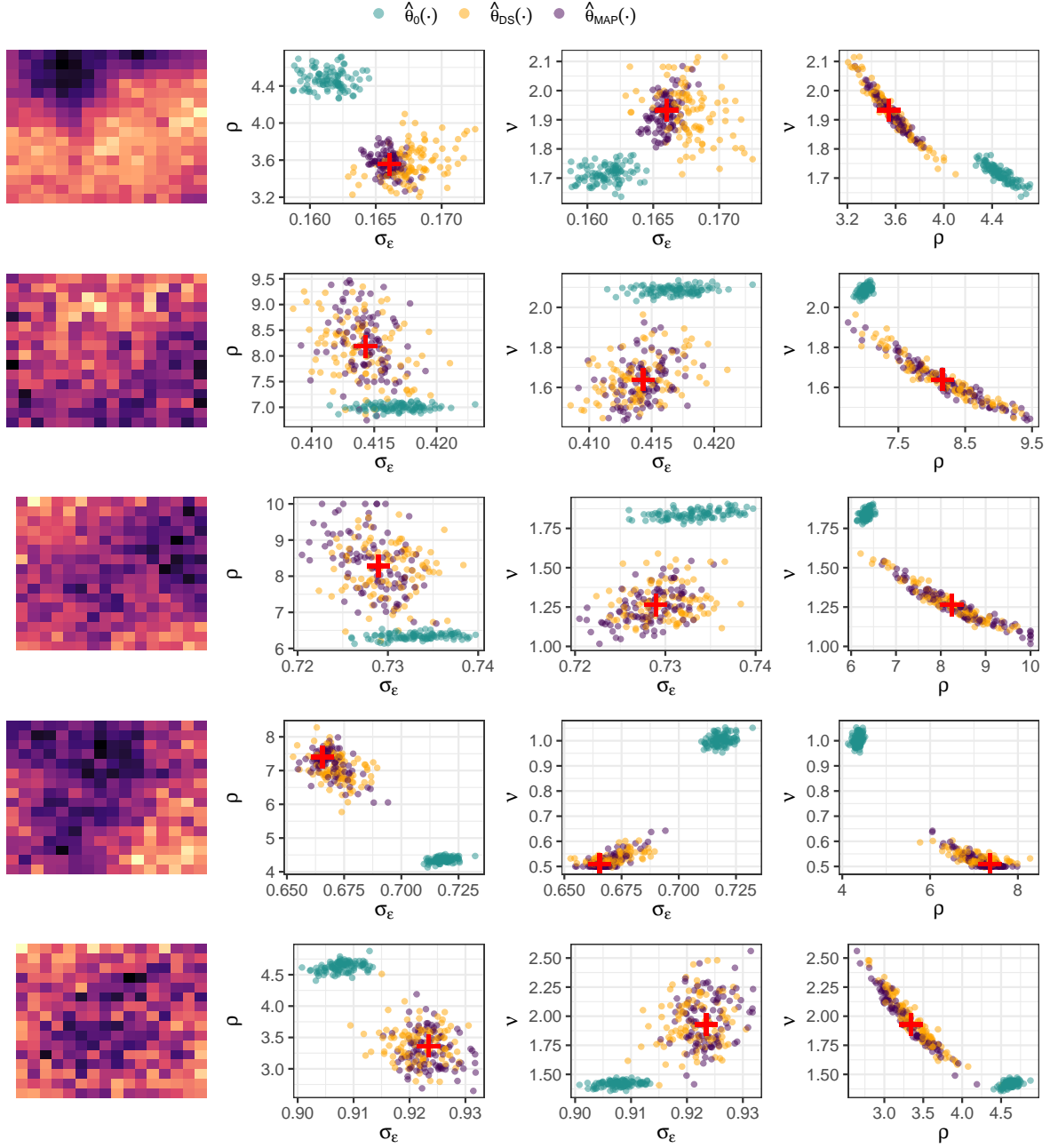


Figure S10: The empirical joint distribution of the estimators considered for the Gaussian process model of Section 4.2 of the main text. Each row corresponds to a randomly chosen element of ϑ_{test} . The left panel of each row shows a single realisation from the model under the true parameters of the given row. Within each of the remaining panels, the true parameters are shown as red crosses, while estimates from $\hat{\theta}_0(\cdot)$, $\hat{\theta}_{\text{DS}}(\cdot)$, and the MAP estimator are shown in green, orange, and purple, respectively. Each estimate was obtained from a simulated data set of size $m = 150$.

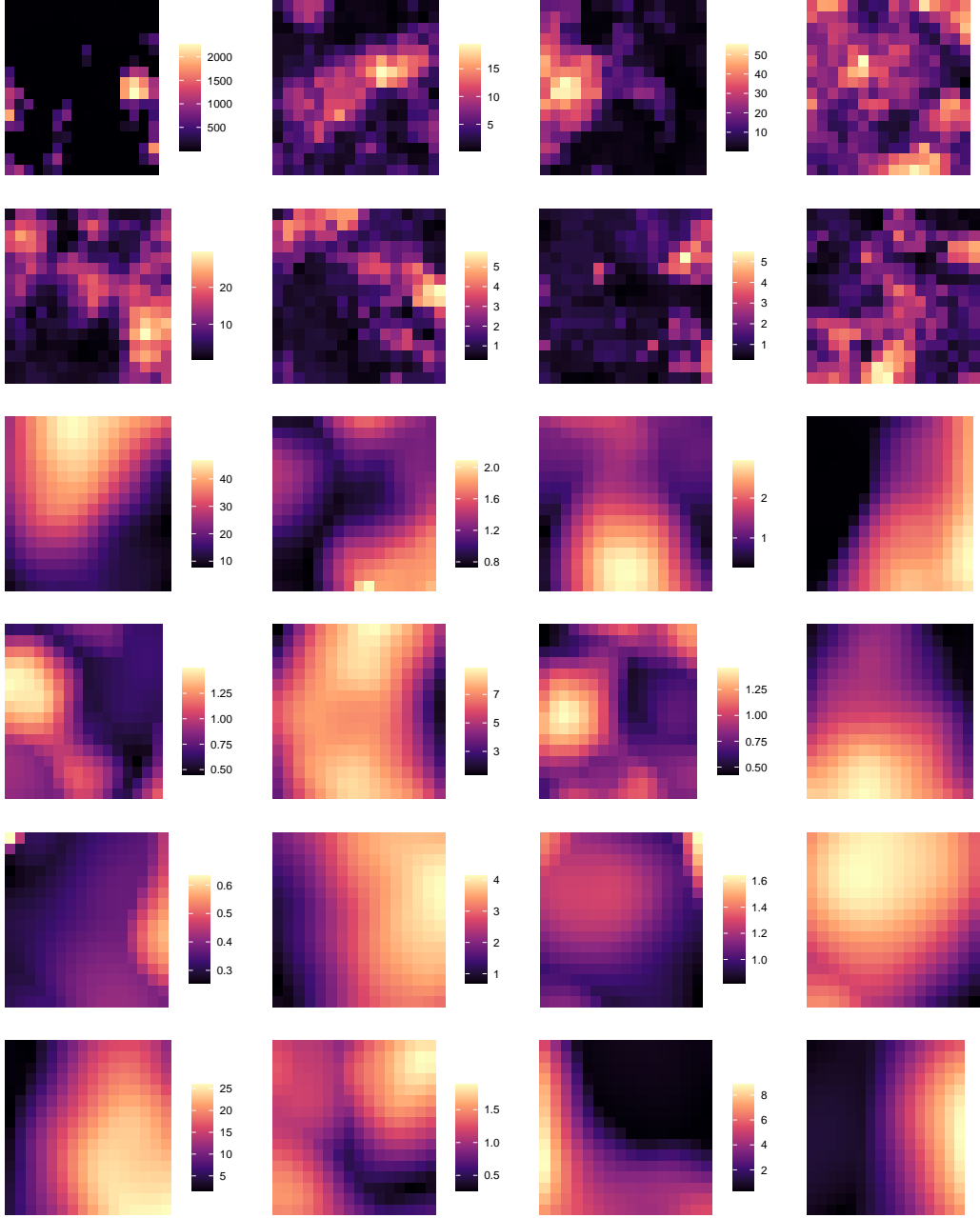


Figure S11: Simulations from Schlather's max-stable model of Section 4.3 of the main text. The figure is divided into three sets of simulations (rows one and two, three and four, and five and six), within which the model parameters are fixed. Within each set of simulations, the dependence structure is similar in all fields, but the magnitude varies considerably.

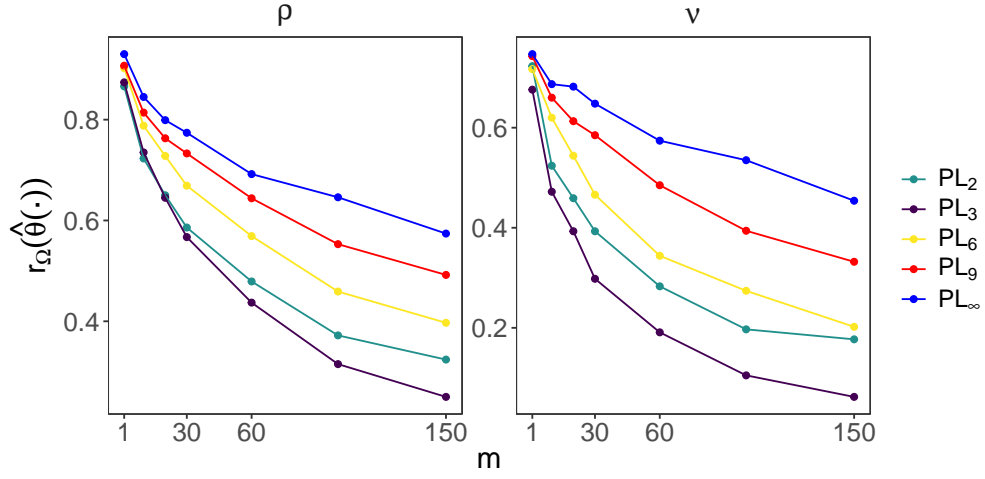


Figure S12: The risk with respect to the 0–1 loss against the number of replicates, m , available for each parameter vector in ϑ_{test} , for several pairwise MAP (PMAP) estimators considered for Schlather’s max-stable model of Section 4.3 of the main text. We denote the PMAP estimator based on the pairwise likelihood (PL) function that uses only a subset of pairs within a fixed cut-off distance, d , by PL_d . In this case, taking $d = 3$ provides the best results.

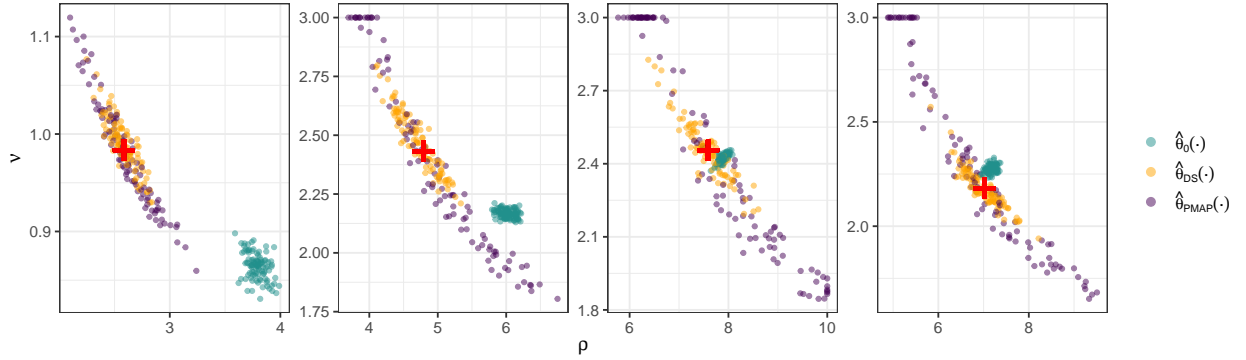


Figure S13: The empirical joint distribution of the estimators for Schlather’s max-stable model of Section 4.3 of the main text. Each column corresponds to a randomly chosen element of ϑ_{test} . Within each panel, the true parameters are shown in red, while estimates from $\hat{\theta}_0(\cdot)$, $\hat{\theta}_{\text{DS}}(\cdot)$, and the PMAP estimator are shown in green, orange, and purple, respectively. Each estimate was obtained from a simulated data set of size $m = 150$.

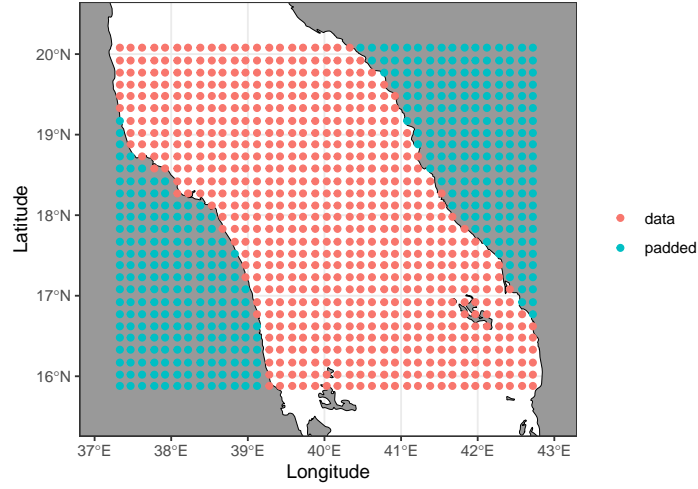


Figure S14: Data and padded regions for the Red Sea application of Section 5 of the main text. Padding is necessary to use a convolutional neural network, which requires a rectangular array.

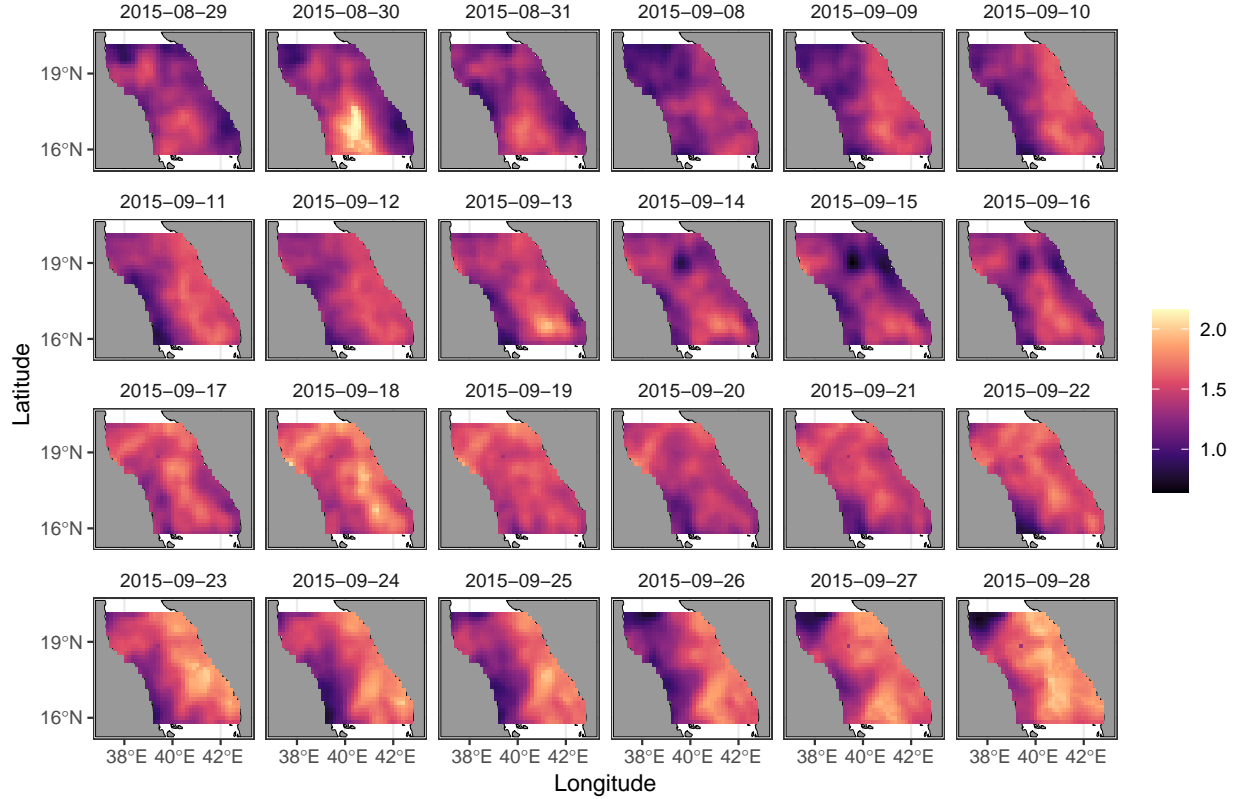


Figure S15: Extreme fields from the year 2015 for the Red Sea data set considered in Section 5 of the main text; here, we show the cube-root of the Laplace-scale data to prevent the colour scale being dominated by outliers. We account for the temporal dependence present in these fields using the block bootstrap approach described in Section S5.

References

- Chan, J., Perrone, V., Spence, J., Jenkins, P., Mathieson, S., and Song, Y. (2018). A likelihood-free inference framework for population genetic data using exchangeable neural networks. In Bengio, S., Wallach, H., Larochelle, H., Grauman, K., Cesa-Bianchi, N., and Garnett, R., editors, *Advances in Neural Information Processing Systems*, volume 31. Curran Associates, Inc.
- Davison, A. C. (2003). *Statistical Models*. Cambridge University Press, Cambridge, England, first edition.
- Dey, D. K. and Yan, J. (2016). *Extreme Value Modeling and Risk Analysis: Methods and Applications*. Chapman & Hall/CRC Press, Boca Raton, FL.
- Gerber, F. and Nychka, D. W. (2021). Fast covariance parameter estimation of spatial Gaussian process models using neural networks. *Stat*, 10:e382.
- Goodfellow, I., Bengio, Y., and Courville, A. (2016). *Deep Learning*. MIT Press, Cambridge, MA.
- Huser, R. (2013). *Statistical Modeling and Inference for Spatio-Temporal Extremes*. PhD thesis, Swiss Federal Institute of Technology, Lausanne, Switzerland.
- Huser, R. and Davison, A. C. (2014). Space-time modelling of extreme events. *Journal of the Royal Statistical Society B*, 76:439–461.
- Rudi, J., Julie, B., and Lenzi, A. (2021). Parameter estimation with dense and convolutional neural networks applied to the FitzHugh-Nagumo ODE. In Bruna, J., Hesthaven, J., and Zdeborova, L., editors, *Proceedings of the 2nd Annual Conference on Mathematical and Scientific Machine Learning*, volume 145 of *Proceedings of Machine Learning Research*, pages 1–28. PMLR.
- Schlather, M. (2002). Models for stationary max-stable random fields. *Extremes*, 5:33–44.
- Subbotin, M. T. (1923). On the law of frequency of errors. *Mathematicheskii Sbornik*, 31:296–301.
- Wadsworth, J. L. and Tawn, J. A. (2022). Higher-dimensional spatial extremes via single-site conditioning. *Spatial Statistics*, 51:100677.
- Wu, Z., Pan, S., Chen, F., Long, G., Zhang, C., and Yu, P. S. (2021). A comprehensive survey on graph neural networks. *IEEE Transactions on Neural Networks and Learning Systems*, 32:4–24.